Remote Sensing of Environment 269 (2022) 112790

Contents lists available at ScienceDirect

Remote Sensing of Environment

journal homepage: www.elsevier.com/locate/rse

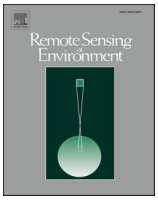

Accurate hyperspectral imaging of mineralised outcrops: An example from lithium-bearing pegmatites at Uis, Namibia

René Booysen [a,b,*], Sandra Lorenz [a], Samuel T. Thiele [a], Warrick C. Fuchsloch [c], Timothy Marais [c], Paul A.M. Nex [b], Richard Gloaguen [a]

[a] Helmholtz-Zentrum Dresden-Rossendorf, Helmholtz Institute Freiberg for Resource Technology, Chemnitzer Straße 40, 09599 Freiberg, Germany
[b] University of the Witwatersrand, School of Geosciences, Jan Smuts Ave 1, 2000 Johannesburg, South Africa
[c] AfriTin Mining, Corner Harries and Fricker Road, Illovo, Sandton, South Africa

ARTICLE INFO

Keywords:
Outcrop sensing
Hyperspectral imaging
Li-bearing pegmatites
Mineral exploration

ABSTRACT

Efficient, socially acceptable and rapid methods of exploration are required to discover new deposits and enable the green energy transition. Sustainable exploration requires a combination of innovative thinking and new technologies. Hyperspectral imaging (HSI) is a rapidly developing technology and allows for fast and systematic mineral mapping, facilitating exploration of the Earth's surface at various scales on a variety of platforms. Newly available sensors allow data capture over a wide spectral range, and provide information about the abundance and spatial location of ore and pathfinder minerals in drill-core, hand samples and outcrops with mm to cm precision. Conversely, the complex geometries of the imaged surfaces affect the spectral quality and signal-to-noise ratio (SnR) of HSI data at these very narrow spatial samplings. Additionally, the complex mineral assemblages found in hydrothermally altered ore deposits can make interpretation of spectral results a challenge. In this contribution, we propose an innovative approach that integrates multiple sensors and scales of data acquisition to help disentangle complex mineralogy associated with lithium and tin mineralisation in the Uis pegmatite complex, Namibia. We train this method using hand samples and finally produce a three-dimensional (3D) point cloud for mapping lithium mineralisation in the open pit. We were able to identify and map lithium-bearing cookeite and montebrasite at outcrop scale. The accuracy of the approach was validated by drill-core data, XRD analysis and LIBS measurements. This approach facilitates efficient mapping of complex terrains, as well as important monitoring and optimisation of ore extraction. Our method can easily be adapted to other minerals relevant to the mining industry.

1. Introduction

The green energy transition is causing a perceived substantial increase in the demand for raw materials and, while recycling rates are improving, new discoveries are required to maintain supply (Gandhi and Sarkar, 2016; Ali et al., 2017). Mapping mineral abundances in an environmentally sensitive manner requires minimally invasive and cost-effective exploration technologies. Geological remote sensing offers a cost-effective way of exploring for mineral resources, and while satellite and airborne imaging are routinely used for exploration targeting, a gap remains at the outcrop scale. Hyperspectral imaging (HSI), typically performed from satellite or airborne platforms, is advantageous for large-scale regional mapping (Kruse et al., 2003). On the other hand, imaging satellite and airborne sensors have ground sampling resolutions ranging from meters up to 10s of meters, and are limited to subdued topography due to their (sub-) nadir viewing angle. Furthermore, detailed understanding of mineralisation is needed to accurately interpret and target potential ore deposits. The solution lies in oblique, ground-based or drone-borne HSI of outcrops that can provide structural and mineralogical maps with mm to cm precision.

Very high resolution imaging of complex geological surfaces is extremely relevant for several critical raw materials such as lithium (Li), rare earth elements (REEs), tungsten and tantalum-niobium, as these are usually found in relatively small deposits up to a size of a few hundred m^2. Lithium, for example, has become a key mineral in the energy transition towards a low-carbon future (Heredia et al., 2020). This

* Corresponding author at: Helmholtz-Zentrum Dresden-Rossendorf, Helmholtz Institute Freiberg for Resource Technology, Chemnitzer Straße 40, 09599 Freiberg, Germany.
E-mail address: r.booysen@hzdr.de (R. Booysen).

https://doi.org/10.1016/j.rse.2021.112790
Received 25 May 2021; Received in revised form 12 October 2021; Accepted 29 October 2021
Available online 10 November 2021

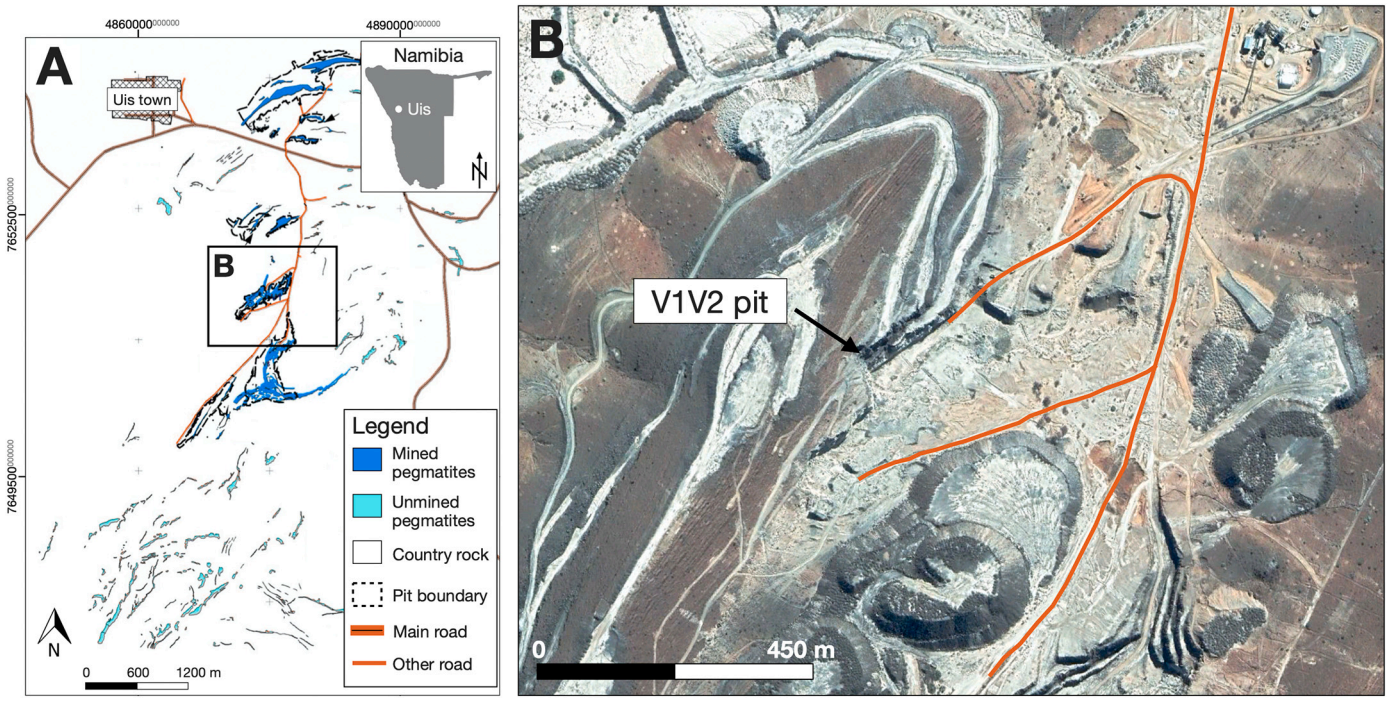

Fig. 1. Study site. (A) Geological map of the Uis Tin mine showing the mapped pegmatites and the location of the main pit. (B) A satellite image of the main V1V2 pit (Google, CNES, Airbus, 2021).

tendency is shown by the EU Commission that changed the status of Li to 'critical' in the 2020 European commission report (EU Commission, 2020). The two primary sources of Li are brine deposits and hard rock deposits such as pegmatites. Pegmatites are intrusive igneous rocks defined by some combination of coarse but variable crystal size, prominent anisotropy of crystal orientation, mineralogical zonation and skeletal, radial and graphic intergrowth crystal habits (London, 2018). The majority of pegmatites have a granitic composition, primarily composed of quartz, feldspar and mica (London, 2018). Most remote sensing studies that have focused on the identification and mapping of Li-bearing pegmatites in the field, use satellite multispectral data. Only a few studies have used hyperspectral data to either identify zones of interest or produce pegmatite maps in the field (e.g., Momose et al., 2011; Cardoso-Fernandes et al., 2020a). Cardoso-Fernandes et al. (2020b) noted that in order to improve lithium exploration, other types of remote sensing platforms should be considered. However, none of these publications described the direct mapping of Li-bearing minerals in exposed pegmatite outcrops. The Uis tin mine located in Namibia, recently declared in excess of 450 Kt of Li-oxide within their V1V2 pegmatite deposit (AfriTin Mining Ltd., 2019), making it an ideal candidate for a proximal HSI approach.

Accurately mapping geological lithologies remains a challenge in inaccessible areas, such as rough terrain or mine sites. Proximal sensing techniques can boost the reliability, safety, and efficiency of geological activities in exploration or during mining activities. It also generates objective, reproducible results and valuable raw data that can be archived, further processed and re-interpreted. The use of ground-based, hyperspectral imaging of outcrops has steadily increased during the last decade, due in part to sensor development and better processing routines. Boesche et al. (2015) and Krupnik and Khan (2019) acquired ground-based, short-wave infrared (SWIR) hyperspectral data to produce two-dimensional (2D) mineral maps. Recently, efforts were made to integrate ground-based hyperspectral imagery with a three-dimensional (3D) surface model for better contextual visualization. Snyder et al. (2016) merged visible and near-infrared (VNIR) ground-based hyperspectral imagery with 3D information to map sedimentary structures. Kurz et al. (2013) and Buckley et al. (2013) developed a workflow for the integration of terrestrial light detection and ranging (LiDAR) point clouds and ground-based hyperspectral scanning. This was one of the first times terrestrial hyperspectral imagery was draped over a LiDAR derived 3D model in order to visualise the hyperspectral data in an accurately scaled representation. Krupnik et al. (2016) registered hyperspectral data with a geometrically accurate LiDAR-derived 3D model to map sedimentological structures based on a custom spectral library built from hand samples. While the 3D digital surface models and point clouds were used to improve visualization, the HSI data remained 2D information with basic spectral and topographical corrections. Lorenz et al. (2018) proposed a new correction workflow that includes atmospheric and topographic corrections for ground-based hyperspectral data with the integration of 3D photogrammetric data to create large-scale so-called "hyperclouds" (i.e., geometrically correct representations of fully corrected hyperspectral datacubes). This was applied by Kirsch et al. (2018) to combine drone-borne and ground-based HSI at the Naundorf quarry in eastern Germany, in order to map geological structures and lithological units for exploration purposes or mine monitoring. This approach is adapted to metric scale structures, but does not account for illumination effects on smaller scales. Due to the weight and cost of full SWIR sensors, drone-borne imaging is currently limited to lightweight sensors covering the VNIR range in operational conditions, and is facing similar challenges (Booysen et al., 2020).

As described earlier, there is no published record of the direct mapping of Li-bearing minerals in pegmatites using hyperspectral imaging (e.g., Momose et al., 2011; Cardoso-Fernandes et al., 2020a). In this paper, we propose a fully 3D, corrected and validated, hyperspectral imaging technique to characterise geological lithologies that can be utilised during mineral exploration or mining activities. We showcase the added value of this multi-scale, hyperspectral remote sensing workflow by directly mapping the internal variability of several Li-bearing minerals in pegmatites being actively mined in Uis, Namibia. For this study, we implement an adapted workflow that includes (1) improved topographic correction based on recent developments on the correction of illumination effects (Thiele et al., 2021); (2) the use of mineralogically based spectral features (e.g., band ratios and minimum

Table 1
Major lithium-bearing minerals with corresponding stoichiometric lithium contents. Li-phases which have been identified at Uis are shown in the first column in bold.

Mineral	Formula	Li_2O	Li
Spodumene	$LiAl(SiO_3)_2$	8%	4%
Petalite	$LiAlSi_4O_{10}$	4%	2%
Lepidolite	$K(Li,Al)_3(Al,Si,Rb)_4O_{10}(F,OH)$	8%	3%
Eucryptite	$LiAlSiO_4$	12%	5%
Amblygonite/montebrasite	$(Li,Na)AlPO_4(F,OH)$	7%	3%
Cookeite	$(Al_2Li)Al_2(AlSi_3O_{10})(OH)_8$	3%	1%
Hectorite	$Na_{0.3}(Mg,Li)_3(Si_4O_{10})(F,OH)_2$	1%	0.5%

wavelength mapping), and; (3) automated feature based mineral identification to map pathfinder and Li-bearing minerals. We combine RGB, VNIR and SWIR data at sample and outcrop scale to provide precise 3D mineral maps, which we validate using laboratory analyses, contiguous spectral measurements covering the VNIR to long-wave infrared (LWIR) range, laser induced fluorescence (LIF), and laser induced breakdown spectroscopy (LIBS).

1.1. Study area

Pegmatites of the Uis Swarm, which are part of the Cape Cross-Uis pegmatite belt, intrude granitic and metasedimentary lithologies of the Neoproterozoic Damara Belt, Namibia (Richards, 1986; Diehl, 1993; Fuchsloch et al., 2018) over an area of ~650 km^2. Several hundred individual pegmatite intrusions have been identified outcropping at the surface (Fig. 1A) (Marais, 2019). Although the petrogenesis of the pegmatites is debated, they are proposed to originate either from the fractionation of *syn*-tectonic granites or post-tectonic anatexis of metasedimentary rocks of the Damara Supergroup (Fuchsloch et al., 2018, 2019a). The pegmatites generally form lens- or sigmoid-shaped intrusions with a north-eastern trend, filling post-tectonic transtensional structures associated with orogenic collapse (Marais, 2019). Intrusion sizes range from cm-scale filled tension gashes to km-long, 100 m wide intrusions (Fuchsloch et al., 2018; Marais, 2019). These show little to no deformation, cross-cut host rock bedding and known structural fabrics within the area, and crystallized at temperatures between 450 and 550 °C (Ashworth et al., 2018).

The Uis pegmatites are granitic lithium-caesium-tantalum (LCT) rare-element pegmatites, varying mostly in terms of accessory phase minerals throughout the swarm, and display no classic mineralogical zonation (Fuchsloch et al., 2018; Fuchsloch et al., 2019a; Fuchsloch et al., 2019b; Marais, 2019). Rock-forming minerals include albite, quartz, orthoclase, muscovite and petalite (Table 1). Accessory phases include cassiterite, columbite-group minerals (CGM), tourmaline, magnetite, ilmenite, beryl, apatite, monazite, lepidolite, cookeite, montebrasite, eucryptite and zircon (Richards, 1986; Fuchsloch et al., 2018; Marais, 2019). Hydrothermal alteration is generally significant, and includes sericitisation, greisenisation and albitisation. Alteration zones, greisens and aplites, are abundant and associated with higher cassiterite and CGM mineral abundances (Fuchsloch et al., 2018).

Our data covers the V1V2 pegmatite of the Uis tin mine (Fig. 1 B), which forms a 1.2 km long, NE-trending, sigmoidal-shaped intrusion dipping between 35° and 50° to the NW (Fuchsloch et al., 2019b). It has sharp, but irregular contacts with the host rock, which are dominantly biotite schist and dark grey quartzite. Initial metallurgical test work (XRD; Fuchsloch, pers. com.) on drill-core identified that some samples contain exclusively petalite as the dominant Li-phase, whereas others contain cookeite (Table 1). Notably, euhedral petalite or feldspar grains are often pseudomorphed completely to cookeite or other Li-bearing clay minerals. Further characterisation of the Li-bearing phases and their distribution is required to assess the feasibility of lithium production from this deposit.

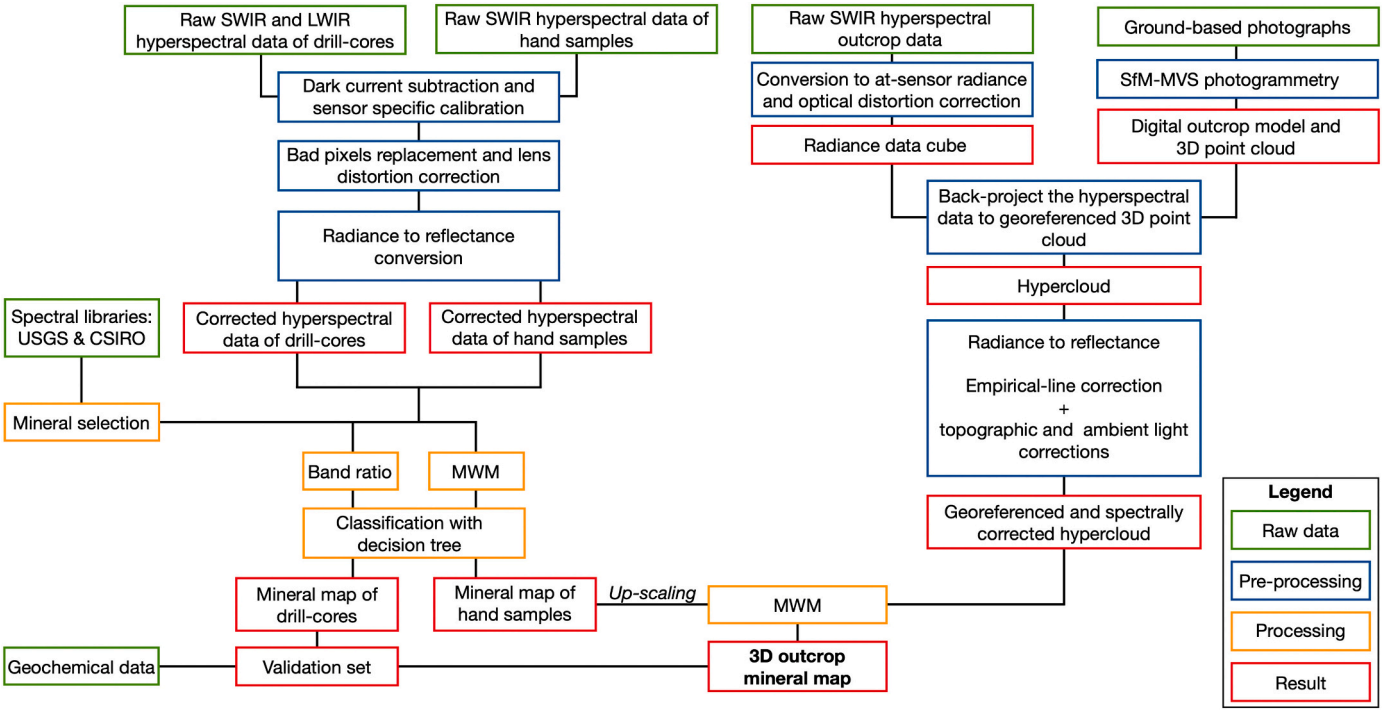

Fig. 2. Workflow showing the processing steps of each dataset and their integration. The workflow starts with four raw data sets; two hyperspectral VNIR-SWIR and LWIR data sets from drill-cores and hand samples acquired in the laboratory, and two data sets acquired in the field consisting of hyperspectral scans and photographs for structure-from-motion, multi-vision-stereo (SfM-MVS) photogrammetry. The data is then corrected and processed for mineral mapping and geological interpretation.

Fig. 3. Set-ups of the hyperspectral sensors in laboratory conditions as well as in the field. (A) The laboratory rock scanner set-up (or SisuRock configuration) with the AisaFENIX and AisaOWL mounted inside. Samples and/or drill-cores are placed on the moving stage in order to be scanned by both sensors. (B) The AisaFENIX mounted to a tripod for in-situ outcrop scanning at the V1V2 open pit. A workstation with a personal computer is required and powered by a mobile generator.

Table 2
The main minerals found in the Uis pegmatites and the range of their characteristic spectral features.

Specifications	Specim AisaFENIX	Specim AisaOWL
Spectral range	380 nm – 2500 nm	7600 nm –12,300 nm
Spectral sampling (FWHM)	VNIR: 3.4 nm SWIR: 5.7 nm	45 nm
Image size (pixels)	384 pixels per line	385 pixels per line
Spatial resolution	Rock scanner: 1.5 mm Outcrop: ~ 8 cm	Rock scanner: 1.5 mm
Approx. Peak-SNR	VNIR: 600–1000:1 SWIR: 1050:1	450:1
Number of spectral bands	Rock scanner: 450 Outcrop scanning: 620	Rock scanner: 96

2. Methodology and equipment

2.1. Data acquisition and pre-processing

We used a unified workflow to image and process the HSI data (Fig. 2). This step is primordial to ensure accurate mineral mapping. The procedure starts with accurate registration and radiometric correction of the imaging data. We then perform spectroscopic and machine learning methods in order to extract relevant mineralogical information. We validate the procedure and assess the accuracy of the results using petrological and mineralogical analysis. The following chapter describes the procedures in detail.

Hyperspectral data was acquired using a tripod mounted Specim AisaFENIX (henceforth referred to as the FENIX) in the main pit at Uis, as well as in the laboratory using both the FENIX and Specim AisaOWL (henceforth referred to as the OWL) mounted on a drill-core scanner/SisuRock configuration (Fig. 3). The FENIX captures data in the VNIR and SWIR regions of the electromagnetic spectrum, while the OWL captures data in the LWIR range (Table 2). Both sensors are pushbroom scanners, with a fixed spectral resolution of 3.5 nm (VNIR), 12 nm (SWIR) and 100 nm (LWIR) respectively, and spatial sampling (GSD) that depends on the distance to the target. The spatial sampling was 1.5 mm in the rock scanner, while at a ground-based field set-up it was ~8 cm (given the viewing distance of ~60 m).

2.1.1. Processing of drill-core data

We scanned 16 m of drill-core and 8 hand samples from the main pit at Uis using both the FENIX and OWL sensors in a SiSuRock scanner configuration (Fig. 3A). This represents an ideal laboratory environment with optimised light source, allowing for a high signal to noise ratio and very high spatial sampling. The raw FENIX and OWL data were processed in accordance with standard procedures using in-house python toolboxes Hylite (Thiele et al., 2021) and Mephysto (Jakob et al., 2017) (Fig. 2). This protocol starts with standard procedures required to produce calibrated data. Dark current data is subtracted to account for pixel sensitivities, and then a sensor specific calibration is applied to convert digital numbers to measured radiance. This calibration is sensor specific and the correction routines are provided by the constructor. Bad or blinking pixels were replaced by the median of the surrounding pixels of the sensor plane. Lens distortion was then corrected to create planimetric images of the scanned samples. Finally, the radiance measurements were converted to reflectance estimates by dividing the data with measurements from a white Spectralon R90 calibration panel (for the FENIX) and brushed aluminium panel (for the OWL). This conversion to reflectance can be considered accurate, given the controlled light source provided by halogen lamps with constant intensity over the entire scan width, flat target surface and nadir configuration of the illumination and sensors. The core samples with a rather low (ambient) temperature received short, but intense thermal illumination during the LWIR measurement. Due to this set-up, the emissivity of the samples can be considered negligible and the reflectivity component dominates the signal, allowing a direct estimation of reflectance using the described workflow.

Four boxes of representative drill-cores were scanned in this manner, each consisting of 4 m of core taken from the pegmatite of the main V1V2 pit. Box 1 contains core samples which were obtained from the shallowest depth and includes the contact between the pegmatite body and the surrounding schist, while box 4 represents the deepest part of the pegmatite body. For the hyperspectral analysis, we selected boxes 1 and 4 because they display clear petrological differences and represent mineralogical endmembers. The geochemical assays by a combination of ICP-MS and ICP-OES analyses at 1 m intervals from a twin borehole provided by AfriTin, indicate that the cores in box 1 contain roughly 2000–2500 ppm Li while those in box 4 contain 3500–4000 ppm of Li.

The distribution of Li-bearing minerals in the drill-cores was confirmed indirectly by assessing Li-content using a handheld laser-induced breakdown spectrometer (LIBS). On selected parts of the core, laser-induced fluorescence (LIF) measurements were conducted to map quartz and feldspars. In the LIF measurement set-up, a high-intensity laser line with a 447 nm excitation wavelength was used to measure

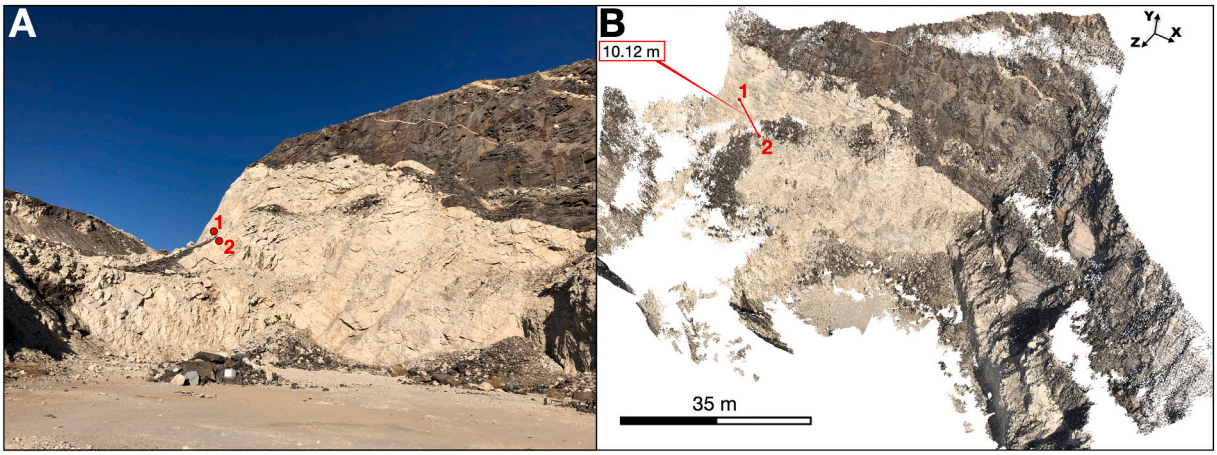

Fig. 4. Geographic positions of pixels in a 2D photograph vs. a 3D point cloud. (A) 2D photograph of the main V1V2 pit indicating the positions of seemingly neighbouring pixels labelled point 1 and 2. (B) 3D point cloud showing the true locations of the pixels and the distance between them.

photoluminescence in the sample under the absence of ambient light. The spectral signal was recorded over the VNIR range using a highly sensitive high-resolution Specim sCMOS-50-V10E hyperspectral line-scanner. The resulting data was dark current corrected and co-registered with the hyperspectral reflectance measurements. Thin sections made from representative parts of the core were used for optical microscopy and petrography to corroborate the mineral maps.

Hyperspectral imaging of cleaned half-cores in the rock scanner provides very accurate mineral spectra that are not totally representative of the spectral signatures of the same rocks in natural conditions (e.g., surface roughness, surface weathering). We therefore scanned hand samples taken from the main pit with the FENIX in the same set-up to acquire data that represent more realistic surface conditions. The information acquired in the laboratory can be used for in-depth investigations and provide contextual information that can be used to map an outcrop (Fig. 2). The pre-processing steps for this data set are the same as for the drill- cores in the SisuRock set-up. The hand samples were sent for X-ray diffraction (XRD) and ICP-AES analysis to determine the bulk elemental and mineralogical compositions and to validate the hyperspectral findings.

2.1.2. Outcrop imaging

LWIR sensors require additional administrative authorization to enter and exit countries, so only the FENIX could be used to acquire outcrop scans in Namibia during the field campaign (Fig. 3B). Three pits were scanned with the FENIX, but, for the sake of simplicity, we only display results of the main V1V2 pit in this paper. The tripod-mounted sensor faced south, sub parallel to the strike of the pegmatite in the main V1V2 pit, viewing the principal vertical mine wall horizontally at a distance of approximately 60 m, resulting in a ground sampling distance of about 8 cm. Eight hyperspectral scenes were acquired during peak sunlight hours, when the vertical face receives maximum illumination, with no cloud coverage, thus maximising signal return. The scene with the best signal return was selected for analysis. A Spectralon SRS-99 white reference panel was placed in the scene with an orientation similar to the imaged outcrop to provide a reference spectra for atmospheric and topographic corrections (Fig. 2).

These corrections require detailed information about outcrop geometry which was captured using a structure-from-motion, multi-vision-stereo (SfM-MVS) photogrammetry workflow, outlined by Carrivick et al. (2016) and James et al. (2017), with 111 ground-based photographs. These were processed using Agisoft Photoscan Professional v. 1.2.5 to generate a dense 3D point cloud of the pit (Fig. 2) containing ca. 50 million points spaced ~3 cm apart. This dense cloud was then georeferenced in CloudCompare v. 2.10 using the iterative-closest point (ICP) algorithm to align the model with a drone-derived, 20 cm resolution, digital elevation model (DEM) provided by AfriTin Mining. A textured 3D mesh was then created from the georeferenced point cloud for visualization.

The hyperspectral ground-based data are acquired by scanning the mine wall using a rotary stage. The used line scanner setup features an internal curved optical distortion across and a barrel distortion along the scanning direction. Both effects were corrected following protocols outlined by Lorenz et al. (2018) after dark subtraction and conversion to radiance (Fig. 2). Pixels located on a vertical wall cannot be georeferenced using a geographic projection, since height (the Z dimension) is the dominant variable in the target position. Furthermore, when visualising 2D hyperspectral data, one pixel on an image may be adjacent to another (Fig. 4A), when in-fact the exact geolocation of the two observed surfaces may be tens of meters apart in three dimensions (Fig. 4B). A 3D environment is therefore necessary to preserve the data content of the HSI data. The hyperspectral data were thus fused with the photogrammetric point cloud using the method described by Thiele et al. (2021). The procedure uses SIFT (Lowe, 1999) feature detection and matching to identify the 3D location of keypoints in the hyperspectral data, which are used to estimate camera position and orientation (pose) using the PnP solver and RANSAC outlier detection implemented in OpenCV. The HSI data were back-projected onto the dense point cloud based on this estimated camera pose to attribute each point with a measured radiance spectra and create a 'hypercloud' (Fig. 2) (Lorenz et al., 2018). This resulted in each pixel being assigned an x, y and z coordinate with spectrum data attached. To convert the data to reflectance, we use an empirical line correction (ELC). A white reference target is placed in the field close to the outcrop, these reference spectra are compared to extracted image spectra of ground targets to estimate the correction factors for each band. The hyperspectral image is converted to surface reflectance by applying those correction factors (Fig. 2). The incident angle of incoming light on an irregular surface (such as a rock outcrop) always varies. This results in varying reflected amounts of radiation being captured by the sensor, causing signal distortions. The incidence angles can be calculated with the 3D point cloud and the amount of selected light can be estimated by determining the surface textures and orientations of an outcrop. Additionally, the bright conditions and reflective nature of the rocks result in significant reflected skylight. In addition, other factors such as adjacency effects (i.e. ambient light) also influence the signal. We modelled the contribution of sunlight and skylight spectra for each pixel, and compensated for shadows (Thiele et al., 2021). We corrected the signal for these distortions during the topographic correction routines to retrieve reflectance (Fig. 2). These corrections are important in order to

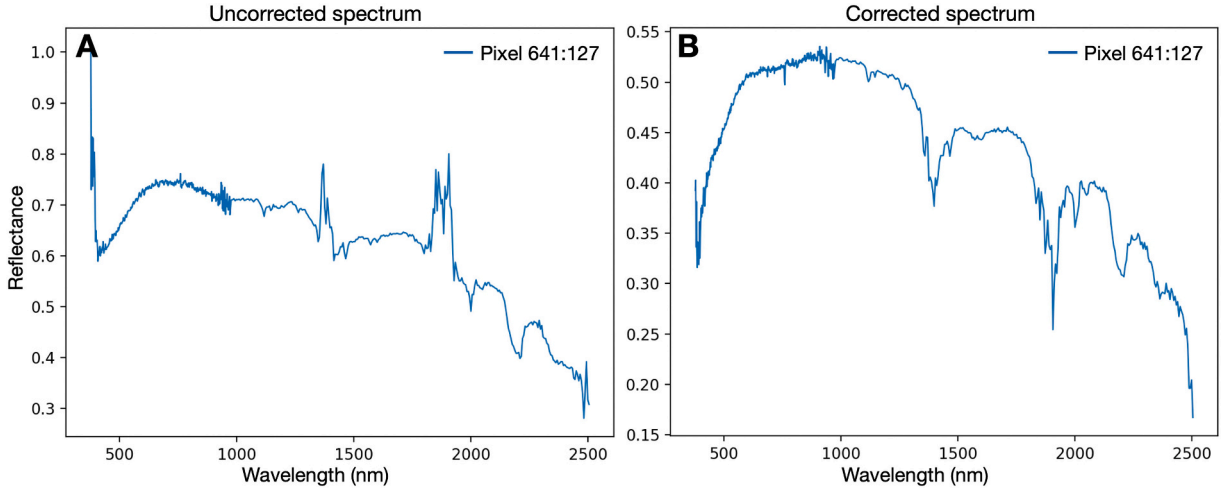

Fig. 5. Example of a spectrum captured during field acquisition with the AisaFENIX showing before and after corrections. (A) Uncorrected spectrum (only ELC applied). (B) After a joint topographic and atmospheric correction.

Table 3
The main minerals found in the Uis pegmatites and the range of their characteristic spectral features.

Minerals in the Uis pegmatites	Characteristic spectral range
Feldspar (predominantly albite and microcline with minor amounts of plagioclase and orthoclase)	LWIR
Quartz	LWIR
Muscovite (and minor amounts of other micas)	SWIR and LWIR
Cookeite	SWIR
Clay minerals (trace amounts)	SWIR and LWIR
Montebrasite (trace amounts)	SWIR

produce a reliable spectrum. The difference in the spectrum between only performing at-sensor corrections and the additional topographic corrections with ambient noise corrections can be seen in Fig. 5. The identification of features specific to minerals can only be done correctly if accurate processing is performed.

2.2. Spectral analysis and mineral mapping

Geological applications of optical spectrometry use wavelength dependent variations in material reflectance to characterise and, ideally, identify mineral phases (Lorenz, 2019; Laukamp et al., 2021). Diagnostic reflectivity variations in the VNIR-SWIR region of the spectra are caused by atomic or molecular vibrations and electron transitions that manifest as distinctive absorption features (Clark, 1999). When investigating minerals and rocks, the most commonly observed spectral features in this range are typically caused by metal ions, water and OH-groups (Hunt, 1977). Thus, minerals containing Fe_3^+, Fe_2^+, AlOH, MgOH or FeOH as well as CO_3^{-2} groups, which include iron-oxides, clays, micas, chlorites and carbonates, can be mapped using these regions of the electromagnetic spectrum. In contrast, fundamental vibration processes are more important in the LWIR region than the overtones and/or combinations observed in the SWIR range, and thus can be used to identify common rock forming minerals, such as quartz, feldspar as well as sheet-silicates such as mica (Lorenz et al., 2019).

Mineral mixtures and relative element concentrations influence characteristic spectral features both in the SWIR and LWIR regions, which can impede straightforward interpretation. LWIR data are particularly difficult to interpret, as characteristic spectral features in this range are also heavily influenced by crystallinity, structural symmetry (e.g., monoclinic or triclinic), degree of ordering (e.g., the ordering of Si and Al) (Harris et al., 1989; Salje, 1994), crystal orientation (Tappert et al., 2013) and grain size. These complex effects make the distinction between different mineral species in this region quite challenging, but also highlight the remarkable amount of useful information that could potentially be extracted and the multiple areas where these techniques could be applied.

Granitic pegmatites are primarily composed of quartz, feldspar and mica (London, 2018), all of which are identifiable in the LWIR region. However, hydrothermal alteration such as the replacement of feldspar with cookeite and Li-clay minerals observed at Uis (Marais, 2019), introduces a diversity of minerals which can be characterised best in the SWIR range. This justifies a combined, multi-sensor approach that may have exploration and industry scale applications.

There has been a recent increase in machine learning techniques, both shallow and deep, in the remote sensing community. These approaches require large labelled datasets to train the classification algorithms. In our case, as with most geological applications, reference data are not available for this specific site. Such a reference would require labelled mineral maps at the outcrop scale, which is difficult to achieve. As a result, we applied a series of bespoke operations to derive meaningful spectral characteristics based on prior knowledge of the defining spectral features of expected minerals stored in the publicly available libraries of the USGS (Kokaly et al., 2017) and CSIRO (Laukamp et al., 2015). As a training set, we used a selection of hand samples extracted from the pit and then mapped relevant minerals in-situ at outcrop scale.

First, the position and depth of diagnostic absorption features were mapped by fitting multiple gaussian functions to hull corrected spectra covering specific spectral ranges. This method is known as minimum wavelength mapping (MWM) (Hecker et al., 2019). These feature position and depth estimates were used to create maps in HSI colour space, where hue is determined by feature position, and intensity (brightness) by absorption depth. This method is effective on high spectral resolution data, where the position of narrow absorption features is sensitive to specific mineral compositions. Additionally, band ratios were computed. A band ratio is the division of one or more spectral bands to derive relative intensity maps that are sensitive to a gradient within a specific spectral range. This technique enhances specific spectral features that can be attributed to certain mineral compositions (Mars and Rowan, 2011).

The principal SWIR active minerals observed in the cores were compared with reference spectra taken from the USGS library. Six spectra representative of the main minerals active in the VNIR-SWIR range were selected by averaging between 20 and 30 pixels of the same mineral identified with MWM. It should be noted that mixtures of these spectra are also present, as grain size is often much smaller than

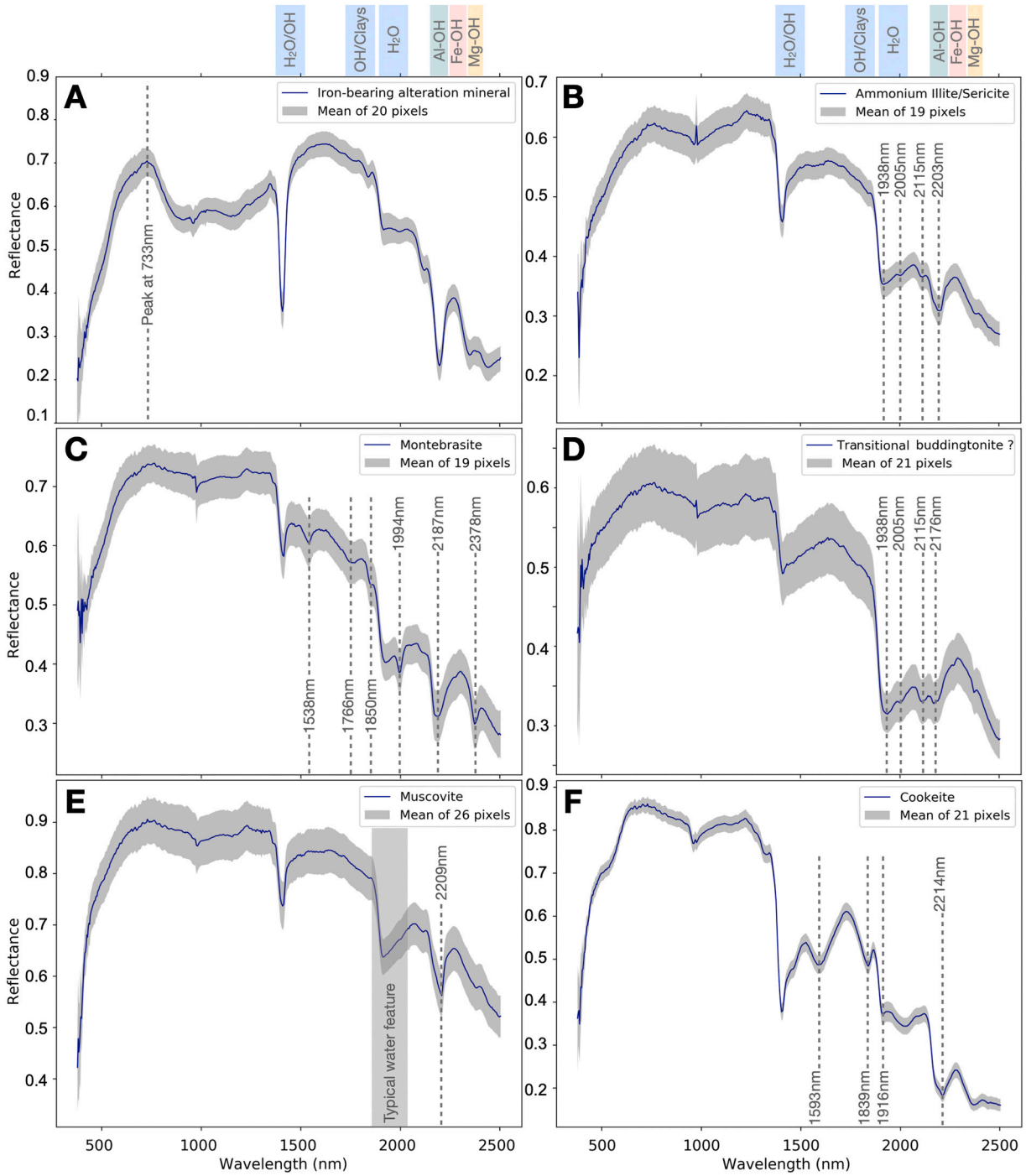

Fig. 6. VNIR-SWIR spectra of minerals from the hand samples captured by the AisaFENIX. (A) Iron-bearing alteration mineral spectrum. (B) Ammonium clay/mica spectrum. (C) Amblygonite group mineral spectrum. (D) Possible buddingtonite spectrum. (E) Muscovite/white mica spectrum. (F) Cookeite spectrum.

the pixel size. We describe the spectral characteristics of the relevant minerals in the appendix. We are confident to be able to map montebrasite, cookeite, muscovite and ammonium-bearing minerals using the SWIR sensor and quartz, albite, microcline, plagioclase and orthoclase using the LWIR sensor (cf. Table 3).

Finally, decision trees were established using spectral endmembers identified in the hand sample dataset based on automatic clustering, and used to map minerals of interest based on their characteristic spectral signatures. This technique uses a tree-like combination of thresholds to filter a feature set into specific classes. The internal nodes or splits are conditions with two or more outcomes, the end nodes or leaves provide the final classification. If each layer consists entirely of binary decisions (e.g., true or false, greater than or less than), the tree is known as a binary decision tree (Kucheryavskiy, 2018). In our case, each input layer consisted of a feature map produced with one of the two appropriate spectral processing methods (i.e., MWM or a band ratio). The pixel-based classification is designed on a true-or-false system that produces a classified mineral map of multiple minerals.

3. Results

3.1. Identification of relevant minerals on the hand samples

Eight representative samples were taken from the main pit. We

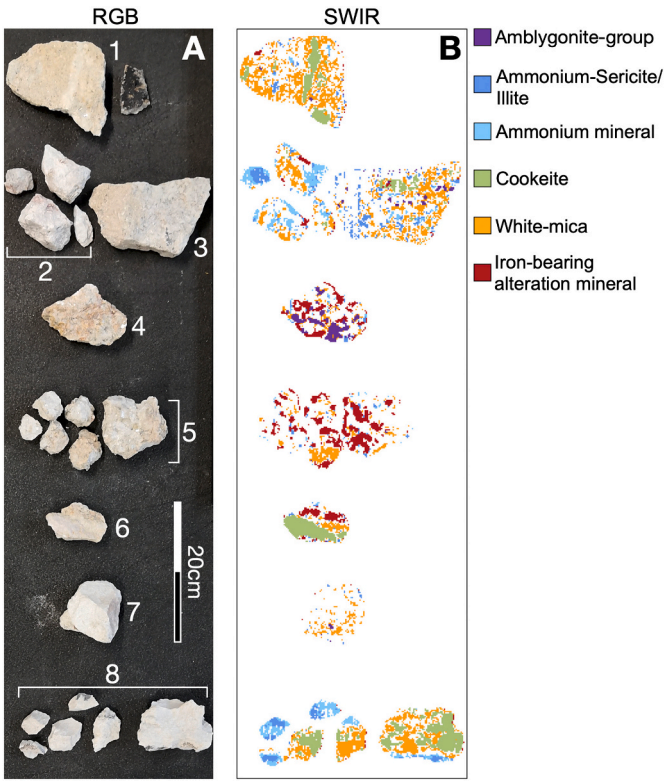

Fig. 7. Decision tree results of hyperspectral data from the hand samples captured by the AisaFenix. (A) RGB photograph indicating the sample number that corresponds to the XRD results in Table 4. (B) Mineral map of the VNIR-SWIR active minerals. The same parameters that were used to map the minerals in the drill-cores were also applied to the hand sample mapping.

selected these samples because they depict the various degrees of mineralisation and alteration found within the exposed V1V2 pegmatite. We observed the same six minerals in the SWIR data of the hand samples that were identified in the drill-core data with minor variability (Fig. 6). The spectra of iron-bearing alteration minerals, montebrasite, muscovite and cookeite were clearly identified (Fig. 6A, C, E and F). In the hand samples however, the iron-bearing alteration mineral spectrum displays spectral characteristics similar to the USGS library's spectrum of lepidolite. Minor amounts of lepidolite have been identified by AfriTin at Uis (Table 1). The ammonium spectra we identified in the hand samples were slightly different from the ammonium spectra observed in the drill-cores. It is evident that there are two types of ammonium-bearing minerals in the drill-cores, one with an AlOH absorption feature and one without this feature (cf. Appendix). However, in the hand samples one of the spectrum contained a deep AlOH absorption feature (Fig. 6B), while the other also contained this feature, albeit less prominently (Fig. 6D). We interpret this observation as a mixture problem; the spectra with the less prominent AlOH feature being a combination of mica/clay and ammonium-bearing feldspar.

These spectral features identified in the hand samples SWIR data set were used in the decision tree to produce a mineral map (Fig. 7). White mica (assumed to be muscovite) is mapped in orange, while the Li-bearing minerals, cookeite and montebrasite, are mapped in green and purple respectively (Fig. 7B). The ammonium-bearing minerals were mapped in dark and light blue, while minor amounts of iron-bearing minerals were mapped in red (Fig. 7B). The mineral map indicates that the highest amount of cooketite was mapped in samples 1, 6 and 8, while sample 4 contained the highest amount of montebrasite (Fig. 7B).

3.2. Outcrop mapping

Based on the spectral information from the hand specimens and validated by the drill-core data, we mapped the entire pit using the fully corrected 3D hypercloud. The spectra between 1370 nm–1480 nm and 1865 nm–2025 nm of the outcrop data cannot be used due to an intense overprint caused by the corrections to remove the effects of atmospheric absorption from water vapour. Therefore, only the absorption features outside of these regions were used to map the various minerals in the main pit (Fig. 8). We used the 2198 nm absorption feature to map the occurrence of AlOH in green (Fig. 8B). Most of the SWIR active minerals found in the pegmatite contain an AlOH feature. The deep AlOH features mapped in darker green are concentrated around the mapped cookeite and montebrasite (Fig. 8B). We used the absorption feature at 1593 nm to map cookeite surface abundances (orange) and the 1538 nm feature to map montebrasite abundances (purple) (Fig. 8C). Both the cookeite and montebrasite are concentrated in spatially localised zones and do not appear to overlap each other. Diagonal, parallel planes of variable mineralisation can clearly be observed in the areas mapped as cookeite and montebrasite (Fig. 8B and C). This repetitive and pervasive layering is oblique to the image raster and cannot be attributed to data processing. This banding is observable on high resolution RGB data as well but not to its full extent.

3.3. Validation with drill-core analysis and geochemistry of hand samples

Observations from thin-section microscopy showed that the rocks consist of complex mineral assemblages. This indicates that at the instrument's spatial resolution each pixel of the hyperspectral images represents various mineral mixtures. The phenomenon produces mixed spectral signatures, resulting in pixels with characteristic features representing different minerals that are active in various parts of the electromagnetic spectrum in the VNIR, SWIR as well as the LWIR regions. This is evident in all three data sets (drill-core, hand samples and outcrop).

As it is challenging to accurately discriminate muscovite from other white micas in the SWIR, we grouped the white micas in one class shown in orange (Figs. 9A and 10A). The cookeite class is displayed in green (Figs. 9A and 10A). The ammonium-bearing minerals were classified as ammonium-sericite/illite and buddingtonite and shown in shades of blue. Minor amounts of iron-bearing minerals and montebrasite are shown in red and purple respectively (Figs. 8A and 9A). In the LWIR, we mapped the alkali feldspars in blues and purple, with orthoclase in light blue and unspecified alkali feldspars in dark blue (Figs. 8C and 9C). Microcline is classified into two groups, one having distinct features is mapped in navy and another with indistinct features, mapped in purple. We classified the plagioclase in a distinct albite class, mapped in orange and distinguished from other, unspecified plagioclase in yellow. Quartz was mapped in two classes, differentiating pixels with deep and shallow absorption features in shades of green (Figs. 9C and 10C). The feature depth can be used as a proxy for the relative abundance (Hecker et al., 2019).

Spatial correlations between the SWIR active minerals and the LWIR active minerals can be observed in the classified mineral maps from box 1 and box 4 (Figs. 9 and 10). From the observation of the decision tree maps, cookeite mapped in the SWIR spatially correlates with the quartz mapped in the LWIR (both are shown in green in the respective maps in Fig. 9A and C; Fig. 10A and C). The ammonium features mapped in the SWIR are shown in blues, and spatially correlate with the alkali feldspars in the LWIR, which are also shown in blue/purple (Fig. 9A and C; Fig. 10A and C). The white mica mapped in the SWIR is shown in orange, and spatially correlates with albite and unspecified plagioclase (Fig. 9A and C; Fig. 10A and C). These associations represent the various alteration styles found as primary pegmatite minerals are progressively altered (and mineralised).

The contact between the schist and pegmatite is clearly distinguished

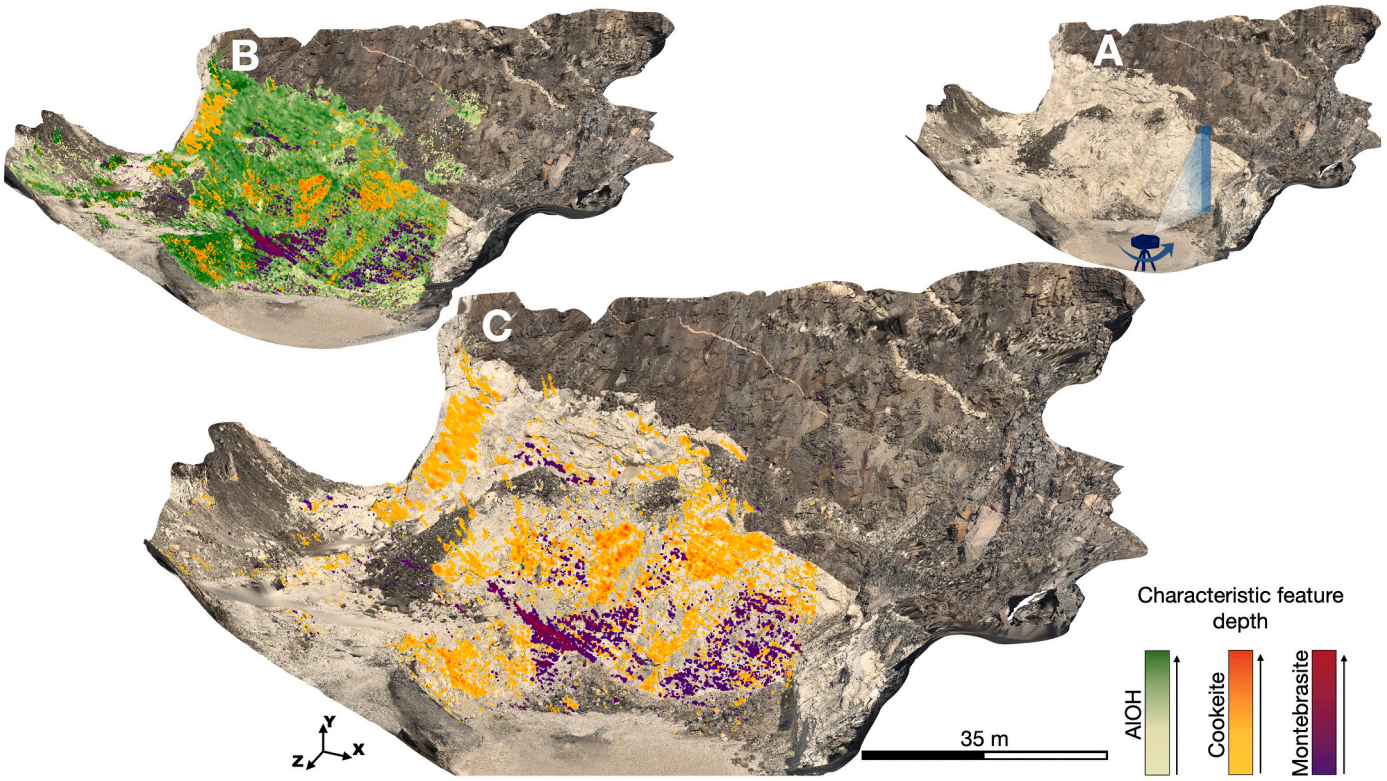

Fig. 8. 3D mineral map of the V1V2 pegmatite body at Uis. (A) RGB 3D model of the V1V2 pit indicating the location of the FENIX sensor. (B) Hypercloud minimum wavelength map showing the mineral abundances overlain onto the 3D model of Uis, cookeite and montebrasite and (C) only the Li-bearing minerals. The colour corresponds to the composition or characteristic mineral absorption feature mapped and the intensity indicates the depth of the feature.

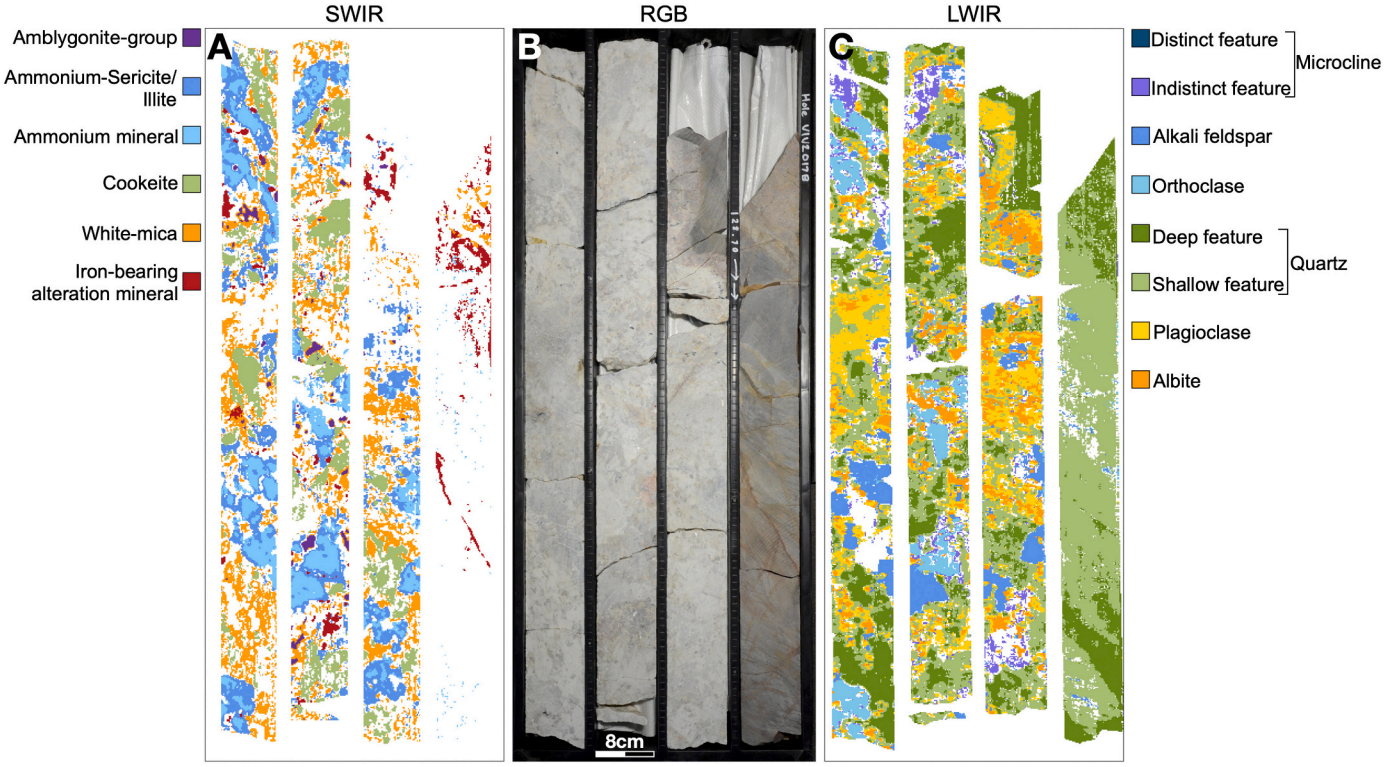

Fig. 9. Decision tree results of hyperspectral data from box 1. Mineral spectra shown in Figs. 12 and 13 of the appendix were used in the mapping methods. (A) Mineral map of the VNIR-SWIR active minerals captured by the AisaFENIX. (B) RGB photograph of box 1. (C) Mineral map of the LWIR active minerals captured by the AisaOWL.

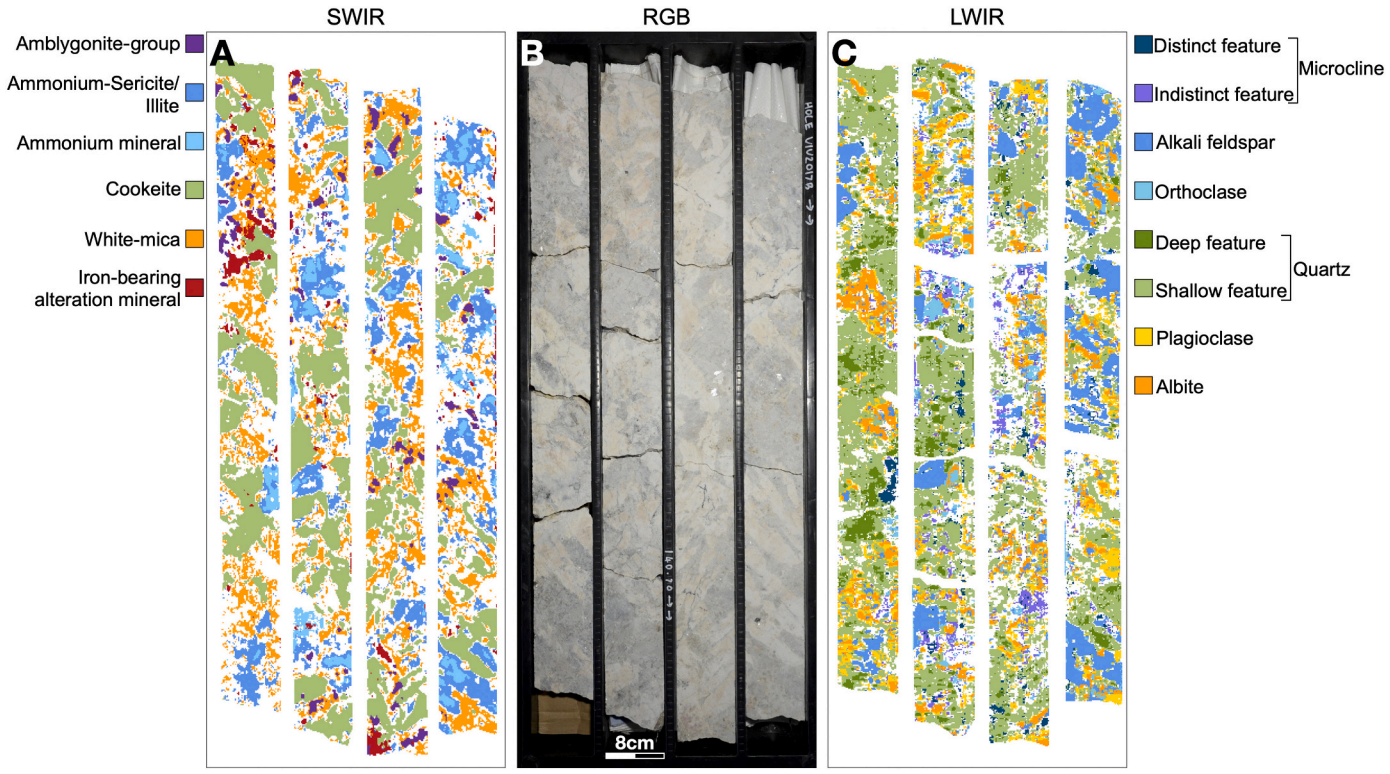

Fig. 10. Decision tree results of hyperspectral data from box 4. Mineral spectra shown in Figs. 12 and 13 of the appendix were used in the mapping methods. (A) Mineral map of the VNIR-SWIR active minerals captured by the AisaFENIX. (B) RGB photograph of box 4. (C) Mineral map of the LWIR active minerals captured by the AisaOWL.

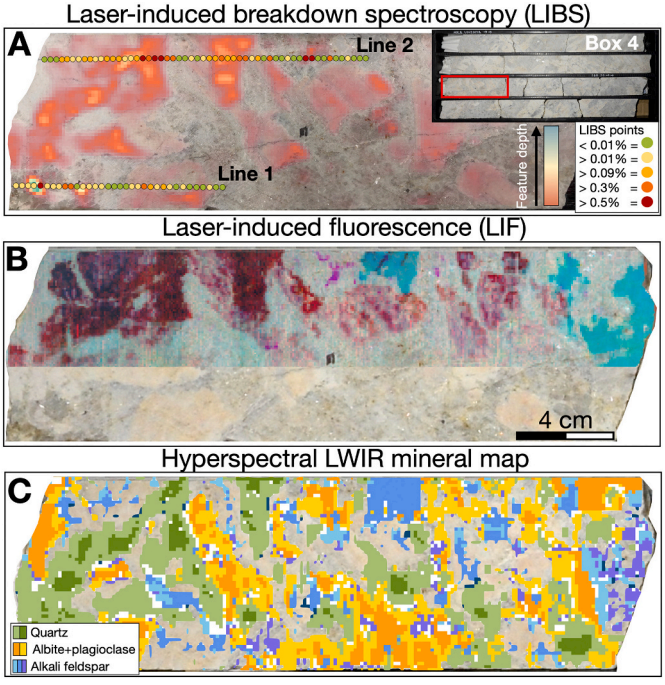

Fig. 11. Validation results. (A) LIBS measurement points overlain onto the minimum wavelength map of Li-bearing minerals (i.e., cookeite and montebrasite). Red LIBS points indicate a Li amount between 0.5% and 1% (cf. Appendix). (B) LIF false colour result highlighting the quartz-rich zones in maroon and alkali-feldspars in light blue (R:440 nm, G:526 nm, B:890 nm). (C) Close-up of the hyperspectral LWIR mineral map showing the quartz, plagioclase and alkali feldspars. (For interpretation of the references to colour in this figure legend, the reader is referred to the web version of this article.)

in box 1 in the leftmost drill-core (Figs. 9A and 10C). The map shows that the schist contains a high proportion of quartz (Fig. 9C). Box 4 displays higher abundances of cookeite and montebrasite compared to box 1 (Figs. 9A and 10A). This corresponds with the geochemical assay results, showing that box 4 contains higher amounts of lithium than box 1. More albite was mapped relative to the unspecified plagioclase in box 4 when compared with box 1 (Figs. 9C and 10C). Additionally, box 4 shows a smaller, disjointed and heterogeneous mineral assemblage in LWIR compared to box 1 (Figs. 9C and 10C).

To validate the mapped Li-bearing minerals (i.e., cookeite and montebrasite), we selected a piece of core from box 4 for point measurements with a handheld LIBS device (Fig. 11A). Descriptions of the instrument, its accuracy and quantitative results can be found in the appendix. We measured at 3 mm intervals along 5 profiles, of which 2 are displayed in Fig. 11A. The 5 chosen profiles are representative of the mineral variability in the cores. The 3 mm sampling allows us to map variations over a short distance relatively fast. The chosen profiles stretch across areas with high abundances of cookeite and montebrasite mapped with MWM. The LIBS measurements correlate strongly with the mapped Li-bearing minerals. Lines 1 and 2 indicated that where we mapped high concentrations of cookeite and montebrasite, the LIBS measured between 0.3% and 1% Li. Areas with low concentrations of Li-bearing minerals showed less than 0.09% Li (Fig. 11A, cf. Appendix). Furthermore, we used laser induced fluorescence on the same sample. Due to the lack of references in the literature we postulate that the feldspars luminesce in blue (mapped in cyan) and the quartz in yellow-green (mapped in red) due to the presence of impurities (e.g., Fe) under laser excitation (Fig. 11B). These results further established the mineralogical complexity of pegmatites. The mega crystals that look like feldspars in RGB are indeed clusters composed of a very complex mineral assemblage of remnant feldspar pieces, quartz, micas and cookeite.

XRD and ICP-AES analyses were done on eight hand samples taken from the pit and were used to validate the spectral abundances in the

Table 4
XRD results (orange) and Li concentration measured with ICP-AES (green) on hand samples taken from the pit. The surface abundances of Li-bearing minerals were estimated on classified hyperspectral data and are shown in blue (cf. Fig. 7). The sample numbers are depicted on Fig. 7.

Sample	1	2	3	4	5	6	7	8
Chlorite-group (%)	2.7	3.3	1.2		1.5		1.2	2.7
Microcline (%)		41.4	16.2					
Muscovite (%)	9.5	8.7	12.4	20.6	31.4		22.9	4.8
Plagioclase (%)		13.5	32.5	28.7	26.9	1.7	19.6	2.0
Albite (%)	35.3							4.1
Beryl (%)				1.3				
Cookeite (%)	5.1	2.8	1.5		2.1	26.6	4.0	2.0
Montebrasite (%)	5.5	1.8	3.8	12.5	2.5		4.4	5.8
Orthoclase (%)								51.1
Quartz (%)	41.9	28.5	32.5	37.1	35.7	71.7	47.9	27.7
Li amount from ICP-AES (%)	0.186	0.111	0.131	0.591	0.095	0.276	0.150	0.573
Surface abundance (%): Montebrasite	0	0	4.01	22.5	0	0	0.5	0
Surface abundance (%): Cookeite	16.2	0	7.37	0	0	55	0	25

hand samples and the drill-cores. All samples contained high amounts of quartz, feldspar and muscovite (Table 4). Quartz abundances are proportional to cookeite (Table 4). The amount of montebrasite is variable in the samples and no correlation with other minerals was observed.

We mapped the highest amount of montebrasite in hand sample 4 (Fig. 7B), this was also confirmed by the XRD results (Table 4). The hand sample decision tree results showed a significant amount of cookeite mapped in sample 6 (Fig. 7B). XRD results indicate the highest amount of cookeite is found in sample 6 (Table 4).

In order to assess the accuracy of the hyperspectral mapping, we compared the total surface abundances calculated using the classified HSI data with the ICP-AES concentrations of Li measured by an external contractor. There is a significant correspondence between the Li concentrations and the estimated amount of Li-bearing minerals. We also found a significant correlation between the hand sample surface Li-bearing mineral abundance and their XRD concentrations. The R^2 coefficients between the surface area % of cookeite and montebrasite (Fig. 7) and their volumetric % given by the XRD results (Table 4) are 0.79 and 0.62 respectively.

4. Discussion

This study is a first of this kind where Li-bearing minerals are directly mapped by means of hyperspectral imaging in an open pit. Geological information about the orebody is usually derived from mineral reports produced from geological surface mapping, sampling and drill-core assays. This however takes time, and does not provide the full spatial extent of mineral occurrences and variances over the exposed extent of the pegmatite body. Virtual outcrop models offer an innovative approach to mapping mineralised zones in an active open pit, allowing for a safer and efficient survey resulting in an objective, geometrically correct and spatially continuous mineral map. By mapping in such a way, geologists can devise an improved sampling strategy for further structural, geochemical, and petrological investigations. This approach is also meant to supplement geological fieldwork by providing a qualitative discrimination of geological domains in order to rapidly direct mining activities in the pit. It may be possible to selectively mine specific areas within the pegmatite based on this kind of data in conjunction with geological mapping and surface surveys (e.g., alteration zones with higher ore grades could be targeted). Ore variability (in terms of mineralogy) is also extremely important for processing. An influx of

mica or clay may severely affect the processing plant. Knowing beforehand the incoming mineralogy allows metallurgists to adjust mineral separation and processing procedures accordingly.

The current equipment set-up requires a generator and portable computers, with sensors weighing 20 kg–40 kg. This makes surveying in remote locations without infrastructure still challenging. This issue is being addressed by the current trend in miniaturisation of hyperspectral sensors. However, it will still take some years to decrease the size of SWIR and LWIR sensors that produce the same quality of data as the current available sensors to be integrated in uncrewed aerial vehicles (UAVs).

In this study, a multi-scale hyperspectral imaging approach allowed us to map the Li-bearing minerals and their spatial variability in pegmatites at three scales. To accurately identify the minerals found within the pegmatites, we imaged the hand samples in the SWIR region and used XRD analysis of the same samples as validation. This data was pertinent in identifying absorption features in order to apply the information to the outcrop scale. We are confident that the minerals are correctly mapped in the hyperspectral data of the hand samples due to the positive correlation seen between the abundance of cookeite and montebrasite mapped on the surfaces of the hand samples and their XRD results. The hyperspectral mapping of the hand samples provides a faster and cheaper estimate of surficial mineral abundance than XRD analysis. The samples can be scanned without any type of sample preparation resulting in a faster turnover of information. Furthermore, with hyperspectral mineral mapping, we can produce a continuous surficial mineral map which does not require additional interpolation.

We were able to identify the presence of ammonium-bearing minerals with the hyperspectral data that were not previously reported in any of the publications and available reports. The detection of ammonium through typical geochemical procedures, such as the methods we applied, is a challenge. However, by using HSI we are able to identify the presence and the spatial distribution of ammonium both in the cores and the hand samples. The presence of ammonium in pegmatites has been observed and described in several studies (e.g., Solomon and Rossman, 1988) and can provide useful information on the type of hydrothermal fluids that may affect the mineralogy of the rocks. Trace amounts of ammonium ion (0.7 mol% NH_4^+ substitution) have been identified from the infrared spectra of alkali feldspars from pegmatites occurring in the southern Black Hills district, South Dakota (Solomon and Rossman, 1988). The spectroscopic data indicate that the ammonium is structurally bound, most likely in the M site of the microcline. These results indicate that ammonium was likely a component of metamorphic fluids present during the anatexis of metasedimentary rocks in the southern Black Hills district (Solomon and Rossman, 1988). This information is currently being assessed by the company geologists to better understand the origins of the different alteration processes due to its association with high Sn and Ta grades within the pegmatites.

Mineral maps produced are purely surface estimates, and cannot directly serve as quantitative concentrations. We used existing spectral libraries (the USGS and CSIRO spectral libraries) to accurately identify the minerals in the pegmatites. However, some mineral spectra are not present in these libraries, making certain expected minerals difficult to identify. In this study, we could not find montebrasite in the existing spectral libraries, and therefore used the reference spectrum of the amblygonite group and compared it with observations made in other pegmatite studies. However, this may still cause confusion when identifying certain minerals. Furthermore, differentiating between different feldspars is still challenging due to the already mentioned nature of spectra in the LWIR, as well as the lack of diversity of feldspar spectra in existing spectral libraries. Most of our assessments to classify the different feldspars were based on studies that investigated the changes in feldspar spectra caused by various parameters (e.g., Salje, 1987; Harris et al., 1989; Salje, 1994;). There is an urgent need for complete mineral libraries from VIS to LWIR that also document the variability of spectral signatures in different mineral forms. In the case of long term monitoring, a site specific spectral library developed from samples acquired within the area and validated with mineralogical analysis such as μXRF, EMP or SEM-MLA would result in optimal mineral classification.

A challenge in correctly identifying minerals in pegmatites can come from a strong overprint due to hydrothermal alterations and recrystallisation that create pseudomorphic crystal textures. The RGB showed large crystal structures that resemble feldspar and quartz, which were in-fact extensively replaced by other minerals. With the hyperspectral imaging, we were able to determine the composition of the secondary mineral assemblages that replaced the original crystals. Taking a hyperspectral imaging approach allowed us to determine the mineral complexity of the pegmatites on a macro-scale. Typically, this type of information is determined by investigating thin sections through detailed mapping, polarized light microscopy, μXRF or electronic microscopy. However, this process is time consuming, laborious and can only cover small areas of either the hand samples or cores, which is difficult to apply to pegmatites due to such large crystal sizes. SWIR and LWIR imaging of the drill-cores served as spectral validation to the hand sample mineral maps, and provided an improved understanding of mineral associations in the pegmatites. By using both VNIR-SWIR and LWIR data, we were able to identify a wide range of relevant minerals. We also produced two mineral maps where the spatial correlation between various minerals are discernible. We were able to map the degree of albitisation associated with smaller, disjointed heterogeneous minerals in the cores (Figs. 9C and 10C) that may indicate a higher degree of alteration by hydrothermal fluids or greisenisation. This type of information makes hyperspectral analyses of drill-cores and hand samples unique in the sense that other typical geochemical analyses cannot rapidly provide information of mineral distribution in the cores or spatial correlation between these minerals. Furthermore, we are confident in the resulting mineral map due to a positive correlation seen between the amount of Li measured by the LIBS on the cores and the mapped Li-bearing minerals.

Capturing ground-based hyperspectral data in the field introduces external effects not present in laboratory conditions. In our case, the extremely bright conditions and very white, reflective lithologies resulted in an intense spectral overprint of atmospheric features in the data. This produced an overall noisy dataset with highly exaggerated water bands that made accurately identifying and mapping certain minerals unreliable. To improve the spectra, we used corrective algorithms to remove or reduce radiometric and geometric distortions based on the work by Lorenz et al. (2018) and Thiele et al. (2021). With the improved spectra, we were able to confidently distinguish the two closely spaced absorption features of montebrasite at ca. 1538 nm and cookeite at ca. 1593 nm. Despite the substantial improvement provided by accurate corrections, outcrop sensing is still impeded by certain limitations. The hyperspectral outcrop data have pixels with an average size of 8 cm. In general, the crystal sizes in the pegmatite range from less than 1 cm up to 6 cm wide (with alteration, some crystal sizes are even smaller), resulting in mixed spectral signatures. Therefore, the mineral surface maps show relative abundances of minerals cookeite and montebrasite intimately mixed with quartz and feldspar.

In many cases, it is also important not only to map the phyllosilicates but also tectosilicates and orthosilicates in the pit itself, for future studies we recommend the use of both LWIR and SWIR instruments for outcrop sensing. In the case of Uis, one of the main challenges is that petalite tends to spectrally resemble feldspars and identifying petalite in hand samples or pit faces is very difficult. Even at thin section scale, the optical properties of petalite are identical to feldspars when no prominent cleavage is observed. The techniques described in this study can therefore significantly aid in the identification of petalite provided a reference spectrum is available. The HSI data can also aid the study of the deposit genesis as it provides mineral maps and thus highlights potential spatial characteristics. In the case of Uis, the mineral maps display a very strong banding. The orientation of the observed layering is sub parallel to the strike of the pegmatite body. These structures have

been observed before and are noted in Marais (2019). Layered aplite and greisens also follow a similar orientation, suggesting that fluid alteration pathways and zones are preferably localised along the internal banded structure of the pegmatite, perhaps also suggestive of multiple magma pulses and a structural regime consistent throughout hydraulic fracturing during the exsolution of a Sn-mineralising aqueous phase.

5. Conclusion and outlook

In this study, we used a multi-scale hyperspectral imaging approach to map Li-bearing minerals and their spatial distribution in pegmatites at three scales. We were able to produce a geometrically correct and spatially continuous 3D mineral map of the main pit. We showed the importance of accurate processing in a 3D space and could directly mapped Li-bearing minerals in outcrops using hyperspectral imaging. The procedures described here can easily be adapted to any ore mineral directly observable in reflectance data or inferred using pathfinder mineral associations. The key lies in accurate geometrical and spectral corrections. We thus demonstrated that despite some limitations, HSI can be an asset for the exploration and optimised extraction of many commodities. The next step would be to incorporate the time component, and with repeated acquisitions and real-time processing to provide 4D models that would allow to monitor the evolution of a geological or environmental target. This is particularly interesting for the assessment of environmental issues that have high temporal variability such as acid mine drainage or a tailings dam breach.

Declaration of Competing Interest

The authors declare no conflict of interest.

Acknowledgment

We are thankful to the Helmholtz-Zentrum Dresden-Rossendorf, Helmholtz Institute Freiberg for Resource Technology as well as the University of the Witwatersrand and the DSI-NRF Centre of Excellence (CoE) for Integrated Mineral and Energy Resource Analysis (DSI-NRF CIMERA) for the support and funding of this project. Opinions expressed and conclusions arrived at, are those of the authors and are not necessarily to be attributed to the CoE. We like to thank AfriTin for their support during field work and for providing us access to the mine site. We would also like to thank the AfriTin team for supplying geological information and geochemical data that aided in this study.

Credit author statement

All the authors contributed to the research, data acquisition and processing as well as the writing of this manuscript.

Appendix A. Appendix

A.1. Identification of key minerals

We used specific spectral characteristics to map the relevant minerals found at the Uis mine (Figs. 12 and 13). We identified six primary SWIR active minerals in the cores and compared them to USGS library spectra. The spectra from the cores represent an average of 20 to 30 pixels of the same mineral (Fig. 12). An iron-bearing mineral was identified in minor amounts within the core samples (referred to as iron-bearing alteration mineral; Fig. 12A) based on diagnostic spectral features in the VNIR caused by characteristic electronic processes involving ferric ($Fe3+$) and/or ferrous ($Fe2+$) iron (Crowley et al., 2003). The diagnostic spectral feature manifests as one or two peaks around 600 nm and 900 nm followed by a broad feature centered around 1000 nm. The position of the peaks and the broad depression can be used to determine the specific mineral species. Thus, this iron-bearing mineral was mapped using a band ratio between 733 and 922 nm.

We identified ammonium-bearing minerals based on distinctive absorption features associated with $NH4+$ at 2005 nm and 2120 nm (Fig. 12 B and D) (Simpson, 2015), and found that two types of ammonium-bearing minerals are present in the cores: One with an AlOH absorption feature at 2192 nm, that we associate with mica (Fig. 12B), and another without, likely to be buddingtonite (Fig. 12D). These two minerals were mapped by identifying the $NH4+$ features in the minimum wavelength maps and the presence/absence of the AlOH feature.

Based on our analyses, and observations by Cardoso-Fernandes et al. (2018), montebrasite (an amblygonite-group mineral) and cookeite display discriminating absorption features between 1500 nm and 2000 nm, as well as absorptions related to AlOH and MgOH bonds (Fig. 12C and F). Montebrasite can be identified based on its discriminating features around 1538 nm, 1766 nm, 1850 and both its AlOH (2189 nm) and MgOH (2378 nm) absorption features (Fig. 12C). Similarly, cookeite can be unequivocally identified using the positions of its characteristic absorption features at 1593 nm and 1839 nm (Fig. 12F). To map montebrasite, we thus used the discriminating feature at 1538 nm and its AlOH and MgOH features. In order to map the cookeite, we used both discriminating absorption features at 1593 nm and 1839 nm as well as the AlOH feature. MWM was sufficient to map cookeite and montebrasite without any doubt as the selected features are highly distinctive.

Muscovite was identified based on its characteristic AlOH absorption feature at 2192 nm, and its typical broad water absorption feature at 2000 nm (Fig. 12E) (Beran, 2002; Scott and Yang, 1997). Hence, spectra containing an AlOH feature but no features associated with other minerals were characterised as muscovite.

We identified six primary LWIR active minerals in the cores and compared them to CSIRO library spectra (when possible). The spectra from the cores represent an average of 20 to 30 pixels of the same mineral (Fig. 13). The main rock forming minerals identified are quartz and multiple feldspars. We were able to identify feldspar end-members present in the cores (i.e., albite, microcline and orthoclase), while the other species were indiscriminately described as plagioclase or alkali feldspars. Where possible, the identified spectra were compared to reference spectra sourced from the CSIRO spectral library (Fig. 13A, C and E). As mentioned earlier, the specific reflectance peak positions and intensities of mineral spectra in the LWIR region are variable. Therefore, we based our mapping not only on minima and maxima positions but also on the relative reflectance difference between representative local maxima and minima. We identified quartz based on its two characteristic peaks between 8000 nm and 9500 nm (Tappert et al., 2013), and mapped its spatial distribution by selecting spectra with a single characteristic spectral minimum occurring around 8620 nm (Fig. 13A).

Based on our own analysis and observations made by Hecker et al. (2010), microcline can display three, characteristic reflectance peaks between 9000 nm and 10,000 nm (Fig. 13C). To map microcline, pixels containing the spectral minima at 9340 nm and 9655 nm between the three peaks, and containing no other minima, were selected. Observations from Salje (1994) and Mauger et al. (2016) indicate that albite can be identified by the two characteristic reflectance peaks between 9200 nm and 10,000 nm with the first peak at 9655 nm typically being higher than the second peak at 9975

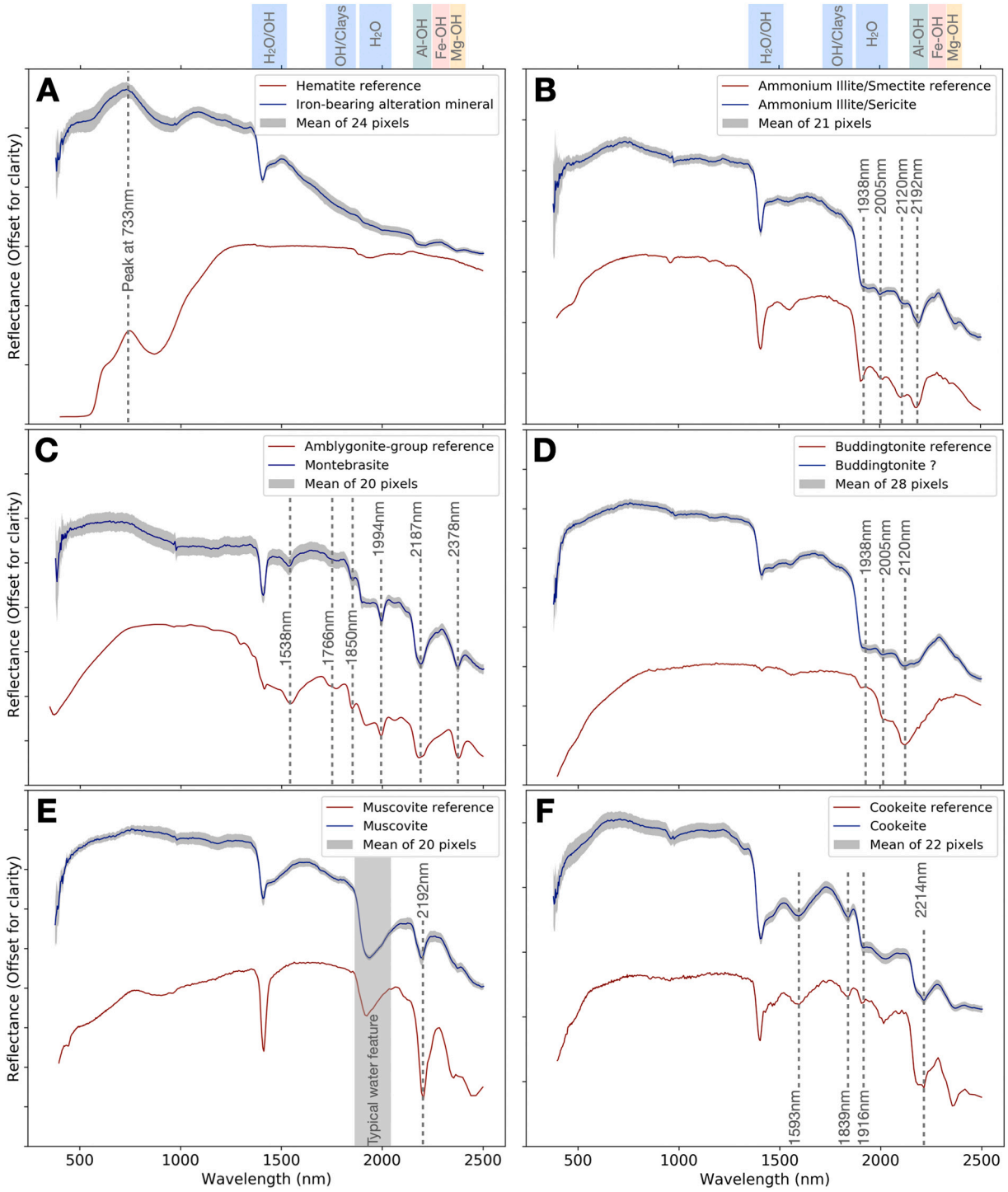

Fig. 12. VNIR-SWIR Spectra of minerals in the drill-cores captured by the AisaFENIX compared with reference spectra taken from the USGS spectral library. (A) Iron-bearing alteration mineral spectrum. (B) Ammonium clay/mica spectrum. (C) Amblygonite group mineral spectrum. (D) Possible buddingtonite spectrum. (E) Muscovite/white mica spectrum. (F) Cookeite spectrum.

nm (Fig. 13E). In order to map albite, we propose to use the position of the minimum between these two peaks at 9790 nm as well as a band ratio to determine the relationship between the peaks.

We found that the other three main representative spectra in the LWIR range were more difficult to classify. Based on observations from Harris et al. (1989), alkali feldspars can display two reflectance peaks between 8500 nm and 10,000 nm, with a local minimum roughly at 9000 nm. With the first reflectance peak being significantly smaller than the second, broader peak (Fig. 13B). To map the alkali feldspars, we identified the local minimum at 8885 nm and additionally we used a band ratio to determine the height relationship between the two peaks at 8706 nm and 9518 nm.

Observations made by Mauger et al. (2016) showed that orthoclase can have two broad reflectance peaks between 8000 nm and 10,000 nm, with the first peak being slightly lower than the second (Fig. 13D). The local minimum between the two peaks, around 9000 nm, is relatively broad as well. We used the position of the local minimum in combination with a band ratio to determine the difference between the intensities of the two peaks to

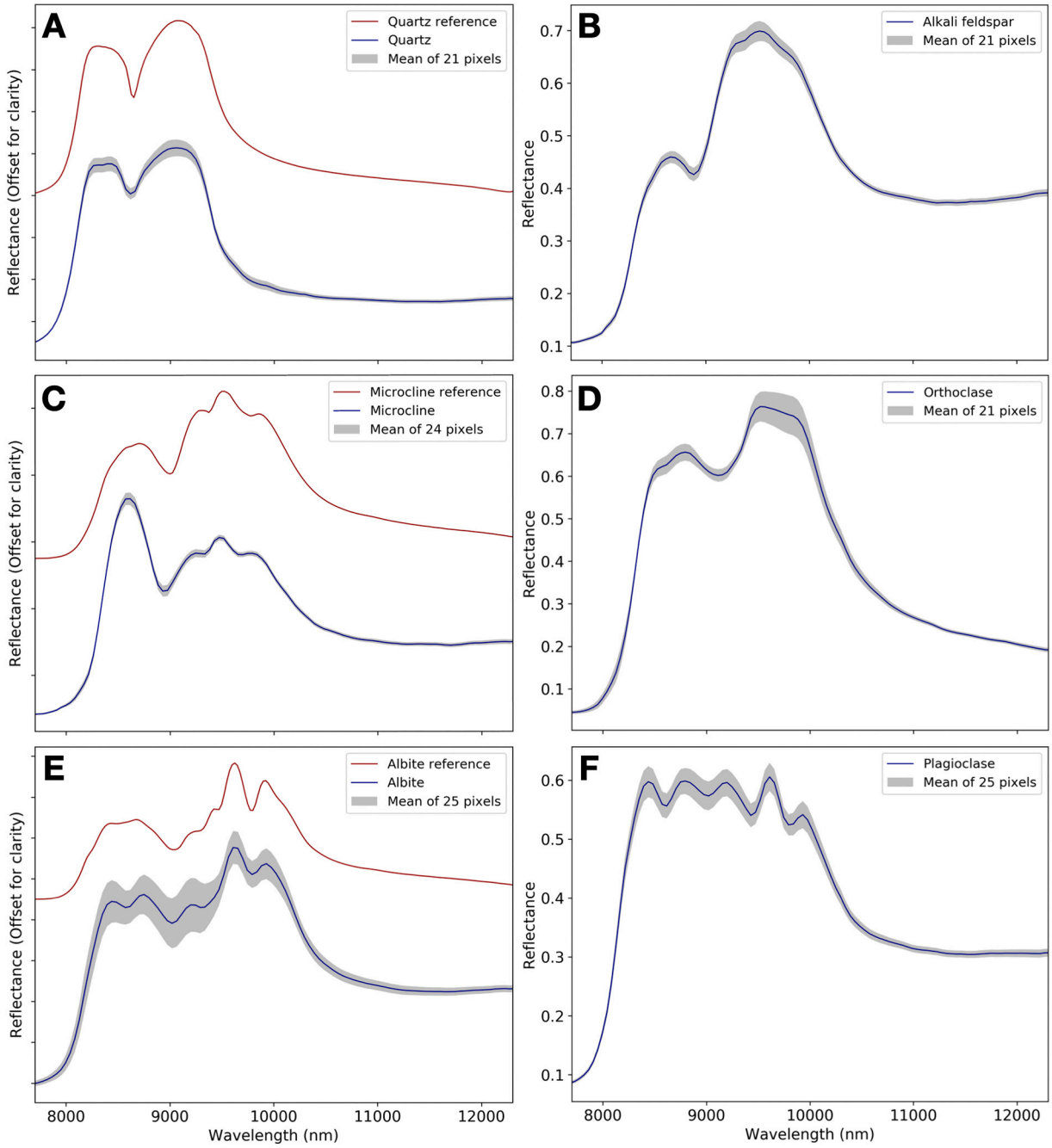

Fig. 13. LWIR spectra of minerals in the drill-cores captured by the AisaOWL compared with available reference spectra taken from the CSIRO spectral library in A, B and C. (A) Quartz spectrum. (B) General alkali-feldspar spectrum. (C) Microcline spectrum. (D) Possible orthoclase spectrum. (E) Albite spectrum. (F) General plagioclase spectrum.

map orthoclase. Plagioclase can display multiple, more narrow reflectance peaks between 8000 nm and 10,000 nm (Fig. 13F) (Salje, 1987). We used the local minima at 9792 nm, 8975 nm and 8620 nm to map plagioclase.

A.2. Validation of the mapped Li-bearing minerals with LIBS

We used the SciAps Z-300 LIBS handheld analyser to validate the mapped Li-bearing minerals in the hyperspectral results. The handheld analyser measures between the range of 190–950 nm and can achieve limits of detection between 2 and 5 ppm for lithium measurements (SciAps Inc., 2019). Table 5 shows the results of the measured points indicated on Fig. 11A.

Table 5
LIBS measurements of each point in lines 1 (blue) and 2 (green) on Fig. 11 A (point numbers are indicated from left to right in each line). The table indicates the measured amount of Li in % as well as the degree of error for each measurement.

Line 1 Point	Li (%)	Li +/- (%)	Line 2 Point	Li (%)	Li +/- (%)
1	0,0199	0,0034	1	0,0075	0,0009
2	0,0164	0,0018	2	0,0020	0,0006
3	0,0173	0,0014	3	0,0090	0,0016
4	0,0117	0,0015	4	0,1401	0,0162
5	0,9055	0,0553	5	0,1637	0,0241
6	0,0153	0,0015	6	0,0126	0,0013
7	0,0158	0,0015	7	0,0122	0,0034
8	0,0125	0,0011	8	0,1839	0,0225
9	0,4293	0,0879	9	0,1677	0,0279
10	0,3924	0,0731	10	0,0146	0,0018
11	0,0077	0,0014	11	0,0130	0,0020
12	0,0203	0,0018	12	0,1497	0,0327
13	0,0115	0,0009	13	0,1436	0,0171
14	0,0135	0,0016	14	0,1935	0,0144
15	0,0126	0,0015	15	0,0108	0,0016
16	0,0030	0,0008	16	0,0106	0,0011
17	0,0027	0,0005	17	0,1723	0,0173
18	0,0019	0,0002	18	0,6776	0,0680
19	0,0084	0,0011	19	0,4979	0,0453
20	0,0131	0,0015	20	0,7041	0,0658
21	0,0130	0,0009	21	0,5241	0,0668
22	0,3025	0,0378	22	0,4431	0,0256
23	0,2046	0,0247	23	0,4729	0,0399
24	0,0134	0,0015	24	0,0028	0,0005
25	0,1334	0,0250	25	0,0046	0,0014
26	0,0142	0,0019	26	0,0141	0,0013
27	0,0063	0,0010	27	0,0094	0,0011
28	0,0125	0,0013	28	0,0147	0,0010
29	0,0089	0,0012	29	0,2061	0,0264
30	0,0054	0,0014	30	0,1447	0,0133
31	0,0045	0,0005	31	0,4301	0,0566
32	0,0129	0,0013	32	0,2720	0,0156
33	0,0036	0,0005	33	0,2566	0,0545
34	0,0077	0,0008	34	0,3657	0,0176
			35	0,4192	0,0231
			36	0,0112	0,0013
			37	0,1469	0,0122
			38	0,0077	0,0012
			39	0,4279	0,0317
			40	0,0072	0,0021
			41	0,0049	0,0010
			42	0,0106	0,0025
			43	0,0078	0,0012
			44	0,0051	0,0007
			45	0,5213	0,0673
			46	0,6066	0,0607
			47	0,0030	0,0005
			48	< LOD	0,2431
			49	0,4234	0,1012
			50	0,0046	0,0005
			51	< LOD	0,1892
			52	0,0120	0,0014
			53	0,0068	0,0004
			54	0,0056	0,0002
			55	0,0098	0,0013

References

AfriTin Mining Ltd., 2019. Maiden JORC resource at Uis. In: Alternative Metal Market. London Stock Exchange. RNS number: 3635M.

Ali, S.H., Giurco, D., Arndt, N., Nickless, E., Brown, G., Demetriades, A., Durrheim, R., Enriquez, M.A., Kinnaird, J., Littleboy, A., Meinert, L.D., 2017. Mineral supply for sustainable development requires resource governance. Nature 543 (7645), 367–372.

Ashworth, L., Kinnaird, J.A., Nex, P.A.M., Erasmus, R.M., Przybylowicz, W.J., 2018. Characterization of fluid inclusions from mineralized pegmatites of the Damara belt, Namibia: insight into late-stage fluid evolution and implications for mineralization. Mineral. Petrol. 112, 753–765.

Beran, A., 2002. Infrared spectroscopy of micas. Rev. Mineral. Geochem. 46 (1), 351–369.

Boesche, N.K., Rogass, C., Lubitz, C., Brell, M., Herrmann, S., Mielke, C., Tonn, S., Appelt, O., Altenberger, U., Kaufmann, H., 2015. Hyperspectral REE (rare earth element) mapping of outcrops—applications for neodymium detection. Remote Sens. 7 (5), 5160–5186.

Booysen, R., Jackisch, R., Lorenz, S., Zimmermann, R., Kirsch, M., Nex, P.A.M., Gloaguen, R., 2020. Detection of REEs with lightweight UAV-based hyperspectral imaging. Sci. Rep. 10 (1), 1–12.

Buckley, S.J., Kurz, T.H., Howell, J.A., Schneider, D., 2013. Terrestrial lidar and hyperspectral data fusion products for geological outcrop analysis. Comput. Geosci. 54, 249–258.

Cardoso-Fernandes, J., Lima, A., Teodoro, A.C., 2018, October. Potential of Sentinel-2 data in the detection of lithium (Li)-bearing pegmatites: a study case. In: Earth Resources and Environmental Remote Sensing/GIS Applications IX, vol. 10790. International Society for Optics and Photonics, p. 107900T.

Cardoso-Fernandes, J., Teodoro, A.C., Lima, A., Mielke, C., Körting, F., Roda-Robles, E., Cauzid, J., 2020a. Multi-scale approach using remote sensing techniques for lithium pegmatite exploration: first results. In: IGARSS 2020–2020 IEEE International Geoscience and Remote Sensing Symposium. IEEE, pp. 5226–5229.

Cardoso-Fernandes, J., Teodoro, A.C., Lima, A., Perrotta, M., Roda-Robles, E., 2020b. Detecting Lithium (Li) mineralizations from space: current research and future perspectives. Appl. Sci. 10 (5), 1785.

Carrivick, J.L., Smith, M.W., Quincey, D.J., 2016. Structure from Motion in the Geosciences. John Wiley & Sons.

Clark, R.N., 1999. Spectroscopy of rocks and minerals, and principles of spectroscopy. Man. Remote Sens. 3 (3–58), 2.

Crowley, J.K., Williams, D.E., Hammarstrom, J.M., Piatak, N., Chou, I.M., Mars, J.C., 2003. Spectral reflectance properties (0.4–2.5 μm) of secondary Fe-oxide, Fe-hydroxide, and Fe-sulphate-hydrate minerals associated with sulphide-bearing mine wastes. Geochemistry 3 (3), 219–228.

Diehl, B.T.M., 1993. Rare metal pegmatites of the Cape Cross – Uis pegmatite belt, Namibia: geology, mineralisation, rubidium-strontium characteristics and petrogenesis. J. Afr. Earth Sci. 17, 167–181.

EU Commission, 2020. Study on the EU's List of Critical Raw Materials – Final Report. European Commission, Brussels, Belgium.

Fuchsloch, W.C., Nex, P.A.M., Kinnaird, J.A., 2018. Classification, mineralogical and geochemical variations in pegmatites of the Cape Cross – Uis pegmatite belt, Namibia. Lithos 296-299, 79–95.

Fuchsloch, W.C., Nex, P.A.M., Kinnaird, J.A., 2019a. The geochemical evolution of the Nb-Ta-Sn oxides from pegmatites of the Cape Cross-Uis pegmatite belt, Namibia. Miner. Mag. 86, 161–179.

Fuchsloch, W.C., Marais, T., Kinnaird, J.A., Nex, P.A.M., 2019b. Characterisation of one of Africa's Giants: the V1-V2 pegmatite, Uis, Namibia. Can. Mineral. 57, 737–740.

Gandhi, S.M., Sarkar, B.C., 2016. Essentials of Mineral Exploration and Evaluation. Elsevier.

Harris, M.J., Salje, E.K., Guttler, B.K., Carpenter, M.A., 1989. Structural states of natural potassium feldspar: an infrared spectroscopic study. Phys. Chem. Miner. 16 (7), 649–658.

Hecker, C., Van der Meijde, M., Van der Meer, F.D., 2010. Thermal infrared spectroscopy on feldspars—successes, limitations and their implications for remote sensing. Earth Sci. Rev. 103 (1–2), 60–70.

Hecker, C., van Ruitenbeek, F.J., Bakker, W.H., Fagbohun, B.J., Riley, D., van der Werff, H.M., van der Meer, F.D., 2019. Mapping the wavelength position of mineral features in hyperspectral thermal infrared data. Int. J. Appl. Earth Obs. Geoinf. 79, 133–140.

Heredia, F., Martinez, A.L., Surraco Urtubey, V., 2020. The importance of lithium for achieving a low-carbon future: overview of the lithium extraction in the 'Lithium Triangle'. J. Energy Nat. Resourc. Law 38 (3), 213–236.

Hunt, G.R., 1977. Spectral signatures of particulate minerals in the visible and near infrared. Geophysics 42 (3), 501–513.

Jakob, S., Zimmermann, R., Gloaguen, R., 2017. The need for accurate geometric and radiometric corrections of drone-borne hyperspectral data for mineral exploration: Mephysto—A toolbox for pre-processing drone-borne hyperspectral data. Rem. Sens. 9 (1), 88.

James, M.R., Robson, S., D'Oleire-Oltmanns, S., Niethammer, U., 2017. Optimising UAV topographic surveys processed with structure-from-motion: ground control quality, quantity and bundle adjustment. Geomorphology 280, 51–66.

Kirsch, M., Lorenz, S., Zimmermann, R., Tusa, L., Möckel, R., Hödl, P., Booysen, R., Khodadadzadeh, M., Gloaguen, R., 2018. Integration of terrestrial and drone-borne hyperspectral and photogrammetric sensing methods for exploration mapping and mining monitoring. Rem. Sens. 10 (9), 1366.

Kokaly, R.F., Clark, R.N., Swayze, G.A., Livo, K.E., Hoefen, T.M., Pearson, N.C., Wise, R. A., Benzel, W.M., Lowers, H.A., Driscoll, R.L., Klein, A.J., 2017. USGS Spectral Library Version 7. In: U.S. Geological Survey Data Series 1035, p. 61. https://doi.org/10.3133/ds1035.

Krupnik, D., Khan, S., 2019. Close-range, ground-based hyperspectral imaging for mining applications at various scales: review and case studies. Earth Sci. Rev. 198, 102952.

Krupnik, D., Khan, S., Okyay, U., Hartzell, P., Zhou, H.W., 2016. Study of Upper Albian rudist buildups in the Edwards Formation using ground-based hyperspectral imaging and terrestrial laser scanning. Sediment. Geol. 345, 154–167.

Kruse, F.A., Boardman, J.W., Huntington, J.F., 2003. Comparison of airborne hyperspectral data and EO-1 Hyperion for mineral mapping. IEEE Trans. Geosci. Remote Sens. 41 (6), 1388–1400.

Kucheryavskiy, S., 2018. Analysis of NIR spectroscopic data using decision trees and their ensembles. J. Anal. Test. 2 (3), 274–289.

Kurz, T.H., Buckley, S.J., Howell, J.A., 2013. Close-range hyperspectral imaging for geological field studies: workflow and methods. Int. J. Remote Sens. 34 (5), 1798–1822.

Laukamp, C., Lau, I.C., Mason, P., Warren, P., Huntington, J., Green, A., Whitbourn, L., Wright, W., Connor, P., 2015. CSIRO Thermal infrared Spectral Library – Evaluation and status report, July 2015.

Laukamp, C., Rodger, A., LeGras, M., Lampinen, H., Lau, I.C., Pejcic, B., Stromberg, J., Francis, N., Ramanaidou, E., 2021. Mineral physicochemistry underlying feature-based extraction of mineral abundance and composition from shortwave, mid and thermal infrared reflectance spectra. Minerals 11 (4), 347.

London, D., 2018. Ore-forming processes within granitic pegmatites. Ore Geol. Rev. 101, 349–383.

Lorenz, S., 2019. The Need for Accurate Pre-processing Data Integration for the Application of Hyperspectral Imaging in Mineral Exploration. PhD thesis. Technische Universitat Bergakadamie Freiberg, Germany, p. 163.

Lorenz, S., Salehi, S., Kirsch, M., Zimmermann, R., Unger, G., Vest Sørensen, E., Gloaguen, R., 2018. Radiometric correction and 3D integration of long-range ground-based hyperspectral imagery for mineral exploration of vertical outcrops. Rem. Sens. 10 (2), 176.

Lorenz, S., Seidel, P., Ghamisi, P., Zimmermann, R., Tusa, L., Khodadadzadeh, M., Contreras, I.C., Gloaguen, R., 2019. Multi-sensor spectral imaging of geological samples: a data fusion approach using spatio-spectral feature extraction. Sensors 19 (12), 2787.

Lowe, D.G., 1999, September. Object recognition from local scale-invariant features. In: Proceedings of the Seventh IEEE International Conference on Computer Vision, vol. 2. IEEE, pp. 1150–1157.

Marais, T., 2019. The Uis Pegmatites: Morphology, Mineralisation and Distribution, with an Emphasis on the V1 and V2 Intrusions. MSc. University of the Witwatersrand, p. 61.

Mars, J.C., Rowan, L.C., 2011. ASTER spectral analysis and lithologic mapping of the Khanneshin carbonatite volcano, Afghanistan. Geosphere 7 (1), 276–289.

Mauger, A.J., Ehrig, K., Kontonikas-Charos, A., Ciobanu, C.L., Cook, N.J., Kamenetsky, V. S., 2016. Alteration at the Olympic Dam IOCG–U deposit: insights into distal to proximal feldspar and phyllosilicate chemistry from infrared reflectance spectroscopy. Aust. J. Earth Sci. 63 (8), 959–972.

Momose, A., Miyatake, S., Arvelyna, Y., Nguno, A., Mhopjeni, K., Sibeso, M., Muyongo, A., Muvangua, E., 2011, July. Mapping pegmatite using HyMap data in southern Namibia. In: 2011 IEEE International Geoscience and Remote Sensing Symposium. IEEE, pp. 2216–2217.

Richards, T.E., 1986. Geological characteristics of rare-metal pegmatites of the Uis type in the Damara orogen, South West Africa/Namibia. In: Mineral Deposits of Southern Africa, 2, pp. 1845–1862.

Salje, E., 1987. Thermodynamics of plagioclases I: Theory of the $I\bar{1} - P\bar{1}$ phase transition in anorthite and Ca-rich plagioclases. Phys. Chem. Miner. 14 (2), 181–188.

Salje, E.K.H., 1994. Phase transitions and vibrational spectroscopy in feldspars. In: Feldspars and their Reactions. Springer, Dordrecht., pp. 103–160

SciAps Inc., 2019. Z-300 LIBS Analyzer. Accessed on 29.09.2021. URL: https://sciaps.com/libs-handheld-laser-analyzers/z-300/.

Scott, K.M., Yang, K., 1997. Spectral reflectance studies of white micas, 439. Australian Mineral Industries Research Association Ltd. Report, p. 35.

Simpson, M.P., 2015, August. Reflectance spectrometry (SWIR) of alteration minerals surrounding the Favona epithermal vein, Waihi vein system, Hauraki Goldfield. In: Proceedings of the AusIMM New Zealand Branch Annual Conference, Dunedin, New Zealand, pp. 490–499.

Snyder, C.J., Khan, S.D., Bhattacharya, J.P., Glennie, C., Seepersad, D., 2016. Thin-bedded reservoir analogs in an ancient delta using terrestrial laser scanner and high-resolution ground-based hyperspectral cameras. Sediment. Geol. 342, 154–164.

Solomon, G.C., Rossman, G.R., 1988. NH_4^+ in pegmatitic feldspars from the southern Black Hills, South Dakota. Am. Mineral. 73 (7–8), 818–821.

Tappert, M.C., Rivard, B., Tappert, R., Feng, J., 2013. Using reflectance spectroscopy to estimate the orientation of quartz crystals in rocks. Can. Mineral. 51 (3), 405–413.

Thiele, S.T., Lorenz, S., Kirsch, M., Contreras Acosta, I.C., Tusa, L., Herrmann, E., Möckel, R., Gloaguen, R., 2021. Multi-scale, multi-sensor data integration for automated 3-D geological mapping. Ore Geol. Rev. 136, 104252.